



HAL
open science

Evolution of the thermohaline structure of one Agulhas Ring reconstructed from satellite altimetry and Argo 2 floats

Rémi Laxenaire, Sabrina Speich, Alexandre Stegner

► **To cite this version:**

Rémi Laxenaire, Sabrina Speich, Alexandre Stegner. Evolution of the thermohaline structure of one Agulhas Ring reconstructed from satellite altimetry and Argo 2 floats. 2019. hal-02340055v1

HAL Id: hal-02340055

<https://hal.science/hal-02340055v1>

Preprint submitted on 30 Oct 2019 (v1), last revised 13 Dec 2023 (v2)

HAL is a multi-disciplinary open access archive for the deposit and dissemination of scientific research documents, whether they are published or not. The documents may come from teaching and research institutions in France or abroad, or from public or private research centers.

L'archive ouverte pluridisciplinaire **HAL**, est destinée au dépôt et à la diffusion de documents scientifiques de niveau recherche, publiés ou non, émanant des établissements d'enseignement et de recherche français ou étrangers, des laboratoires publics ou privés.

1 **Evolution of the thermohaline structure of one Agulhas**
2 **Ring reconstructed from satellite altimetry and Argo**
3 **floats**

4 **R. Laxenaire^{1*}, S. Speich¹ and A. Stegner¹**

5 .
6 ¹Laboratoire de Météorologie Dynamique, UMR 8539 École Polytechnique, ENS, CNRS, Paris, France

7 **Key Points:**

- 8 • Lagrangian reconstruction of an Agulhas Ring sampled by an Argo float for more
9 than 1.5 years
10 • In situ evidence of the subduction of an Agulhas Ring
11 • The reconstructed Agulhas Ring is characterized by two mode water cores

*Current affiliation: Center for Ocean-Atmospheric Prediction Studies, Florida State University, Tallahassee, Florida, USA

Corresponding author: Rémi Laxenaire, rlaxenaire@fsu.edu

Abstract

The transfer of Indian Ocean thermocline and intermediate waters into the South Atlantic *via* the Agulhas leakage is generally believed to be primarily accomplished through mesoscale eddy processes, essentially anticyclones known as Agulhas Rings. Here we take advantage of a recent eddy tracking algorithm and Argo float profiles to study the evolution and the thermohaline structure of one of these eddies over the course of 1.5 years (May 2013–November 2014). We found that during this period the ring evolved according to two different phases: During the first one, taking place in winter, the mixing layer in the eddy deepened significantly. During the second phase, the eddy subsided below the upper warmer layer of the South Atlantic subtropical gyre while propagating west. The separation of this eddy from the sea surface could explain the decrease in its surface signature in satellite altimetry maps, suggesting that such changes are not due to eddy dissipation processes. It is a very large eddy (7.1×10^{13} m³ in volume), extending, after subduction, from a depth of 200–1200 m and characterized by two mode water cores. The two mode water cores represent the largest eddy heat and salt anomalies when compared with the surrounding. In terms of its impact over one year, the north-westward propagation of this long-lived anticyclone induces a transport of 2.2 Sv of water, 0.008 PW of heat, and 2.2×10^5 kg s⁻¹ of salt. These results confirm that Agulhas Rings play a very important role in the Indo-Atlantic interocean exchange of heat and salt.

1 Plain Language Summary

The transfer of the Indian Ocean waters to the South Atlantic Ocean is generally believed to be primarily accomplished through anticyclonic eddies known as Agulhas Rings. There have been various studies investigating these eddies from sparse in-situ and satellite observations. Here we take the advantage of the complementary information provided by eddies detected from satellite maps and free-drifting profiling floats measuring the upper 2000 m of the ocean, to reconstruct the internal structure of one of them. This reconstruction shows that this Agulhas Ring quits the surface layer and slowly sinks into the subsurface as it drifts westward into the Atlantic Ocean. The ring is a very large eddy extending down to 1200 m of depth and characterized by two cores showing temperature anomalies up to 4°C when compared with the surrounding South Atlantic waters. These results confirm that Agulhas Rings play a very important role in the Indo-Atlantic interocean exchange of heat and salt.

2 Introduction

Mesoscale eddies are ubiquitous in the World Ocean (Chelton et al., 2007, 2011). Their energy generally exceeds that of the mean flow by an order of magnitude or more (Stammer, 1997; Wunsch, 1999) and they are thought to have a major impact on the spreading of hydrological properties by advecting them for considerable distances and over long periods. In particular, their influence is seen as key in the transfer of heat, salt, mass, and biogeochemical properties across the World Ocean (McWilliams, 1985).

Over the last 25 years, satellite altimetry has provided a regular, global, high-resolution monitoring of sea level and ocean circulation variations (Morrow & Le Traon, 2012). These data constitute a precious time series with regular spatial sampling capable of recovering around 60% of the variability in the 65 to 300 km mesoscale band (Pujol et al., 2016). For this reason, they allow us to quantitatively investigate the upper ocean dynamics, and they have been shown to be particularly well suited to the study of mesoscale eddies (e.g., Chelton et al., 2011).

Since the early period of satellite altimetry, because of the large extent and intense altimetry signal of Agulhas Rings, various studies have focused on these Rings and their spatio-temporal evolution (e.g., Byrne et al., 1995; Gründlingh, 1995; Schouten et al., 2000; Dencausse et al., 2010; Beron-Vera et al., 2013; Froyland et al., 2015; Wang et al., 2015, 2016; Guerra et al., 2018; Nencioli et al., 2018). Agulhas Rings are mesoscale anticyclones spawned south of Africa by the South Indian western boundary current, the Agulhas, at its Retroflexion. They are large (100 to 400 km diameter) rings of Agulhas Water that enter the Cape Basin southwest of Africa, before moving westward across the South Atlantic Ocean (e.g., Byrne et al., 1995; Schouten et al., 2000; Biastoch et al., 2009; Guerra et al., 2018; Laxenaire et al., 2018). The evolution and fate of Agulhas Rings are important aspects, since these rings are thought to account for an significant percentage of Indian water leakage into the Atlantic (e.g., Gordon & Haxby, 1990; Goni et al., 1997; A. Doglioli et al., 2006). This leakage impacts the Atlantic Meridional Overturning Circulation (AMOC) and the related meridional transport of heat, freshwater, and biogeochemical properties, by influencing its strength (Weijer et al., 1999, 2002; van Sebille & van Leeuwen, 2007), stability (Weijer et al., 2001) and variability (Biastoch et al., 2008; Biastoch & Böning, 2013). Satellite data give access to the evolution of the surface properties of these eddies (e.g., Byrne et al., 1995; Schouten et al., 2000; Lehahn et

76 al., 2011; J. Souza et al., 2014; Froyland et al., 2015; Guerra et al., 2018; Laxenaire et
77 al., 2018). In particular, the above-mentioned studies show that the surface signature
78 of Agulhas Rings decreases dramatically west of the Agulhas Retroflection and across
79 the southern Cape Basin, and continues to decrease gradually across the South Atlantic
80 Ocean (e.g., Froyland et al., 2015; Guerra et al., 2018; Laxenaire et al., 2018). However,
81 the majority of the previous studies based on satellite altimetry and with the aim of re-
82 covering the complete trajectories of one or more Agulhas Rings were not able to track
83 all of them back from their area of Retroflection documenting their first detection in the
84 vicinity of the Cape Basin (e.g., Byrne et al., 1995; Lehahn et al., 2011; J. Souza et al.,
85 2014; Guerra et al., 2018).

86 This is most likely due to the non-consideration by previous studies of the com-
87 plex nature of Agulhas Ring trajectories that undergo many eddy splitting and merg-
88 ing events (Schouten et al., 2000; Dencausse et al., 2010; Kersalé et al., 2018; Laxenaire
89 et al., 2018). For example, studying Agulhas Rings in the Cape Basin, Dencausse et al.
90 (2010) showed that the number of these eddies entering the Basin is multiplied by a fac-
91 tor of two when considering eddy splittings. Moreover, when focusing on the evolution
92 and dissipation of three specific Agulhas Rings, Nencioli et al. (2018) observed a merg-
93 ing of two of them in the vicinity of the South Atlantic Ocean. Consequently, these in-
94 teractions, impacting the pattern of the eddy evolution and dissipation, are important
95 if we are to understand the mechanisms of ocean circulation and how Agulhas Rings in-
96 fluence the Earth’s climate. Indeed, in the published literature it has been documented
97 how Agulhas Ring surface properties change and how their disappearance from satellite
98 altimetry maps is often associated with eddy dissipation processes, albeit direct obser-
99 vations of the latter are lacking. On the other hand, when these eddies are tracked over
100 longer distances and for longer periods, and explicitly taking into account eddy merg-
101 ings and splittings (Laxenaire et al., 2018), intense variations of their surface properties
102 appear to be intimately correlated with such events.

103 Another limitation of satellite observations is that they do not provide informa-
104 tion about the eddy vertical structure and how this evolves en route. Agulhas Rings have
105 only been sampled occasionally by *in situ* observations from ships in the Cape Basin (e.g.,
106 Gordon et al., 1987; Duncombe Rae et al., 1992; van Ballegooyen et al., 1994; Duncombe Rae
107 et al., 1996; Arhan et al., 1999; Garzoli et al., 1999; McDonagh et al., 1999; Schmid et
108 al., 2003; Gladyshev et al., 2008; Arhan et al., 2011; Casanova-Masjoan et al., 2017), in

109 the Southeast Atlantic (M. S. McCartney & Woodgate-Jones, 1991; Arhan et al., 1999),
110 or from Argo profiling floats (J. M. A. C. Souza et al., 2011; Nencioli et al., 2018). How-
111 ever, with the exception of the observations reported in Nencioli et al. (2018), J. M. A. C. Souza
112 et al. (2011) and Arhan et al. (1999), Agulhas Rings have not been sampled by in situ
113 observations farther west of the Southeast Atlantic, nor has it been possible to evalu-
114 ate accurately their internal evolution from the Agulhas Retroflexion onward. Concern-
115 ing this last point, Schmid et al. (2003) and Nencioli et al. (2018) reported on the en-
116 route evolution of Agulhas Rings. Schmid et al. (2003) discussed an Agulhas Ring sam-
117 pled twice, at six-month intervals, in the southern Cape Basin which showed an intense
118 change of the upper-layer eddy properties (essentially in terms of temperature and den-
119 sity, very likely due to strong seasonal air-sea interactions) and a freshening of interme-
120 diate waters. Nencioli et al. (2018) also considered the intense variation of properties in
121 the upper 200 m of an Agulhas Ring crossing the South Atlantic and discussed the mod-
122 ifications in the internal structure of this eddy. Moreover, the internal structure of this
123 eddy was characterized by a subsurface core of homogeneous water that the authors iden-
124 tified as Mode Waters (MWs), in line with previous observations of subsurface intensi-
125 fied structures discussed by Arhan et al. (1999).

126 MWs are thick layers of homogeneous subsurface waters whose existence is thought
127 to depend, as a precondition, on the formation of deep mixed layers (e.g., Hanawa & Tal-
128 ley, 2001). MWs have been identified in every ocean basin, always on the warm side of
129 a current or front (e.g., M. McCartney, 1977; M. S. McCartney, 1982; Hanawa & Tal-
130 ley, 2001). They are generally distributed below the surface far beyond their formation
131 areas. Among these are Western Subtropical Mode Waters (WSTMW) usually associ-
132 ated with subtropical gyres, and Subantarctic Mode Waters (SAMW) associated with
133 the subpolar fronts on the poleward boundaries of the southern hemisphere subtropical
134 gyres (e.g., M. McCartney, 1977; Hanawa & Talley, 2001). MWs are correlated with large
135 surface heat loss from the ocean and their low potential vorticity arises as a result of con-
136 vection (e.g., Hanawa & Talley, 2001). Various MWs in the South Atlantic are discussed
137 in the literature. Of these, Provost et al. (1999) documented from repeated hydrographic
138 cruises two types of MW: the South Atlantic Subtropical Mode Water (SASTMW) found
139 in the western subtropical gyre and the South Atlantic Eastern Subtropical Mode Wa-
140 ter (SAESTMW) observed at the eastern edge of the subtropical gyre. Sato and Polito
141 (2014) introduced a new definition of SASTMW by analyzing Argo float data. Using a

142 clustering method they found three different varieties of SASTMW that differed in their
143 hydrological properties and geographical location. These do not correspond completely
144 with Provost et al. (1999)'s SASTMWs definition as they are defined from many more
145 vertical profiles and over a larger area of the South Atlantic. It should be noted here that,
146 using the eddy database from Chelton et al. (2011), Sato and Polito (2014) checked whether
147 SASTMWs were correlated with the presence of mesoscale eddies. They did not find a
148 high correspondence. However, when these authors did observe a correspondence between
149 SASTMW and eddies, they found that 75% of them were anticyclones.

150 Very recently, de Souza et al. (2018) described the origin of South Atlantic MWs
151 by decomposing thermocline waters as a product of the mixing of different MW varieties.
152 They identified, among others, a particular SASTMW that is located along the Agul-
153 has Rings main route where they are an important contributor of thermocline water. In
154 addition, de Souza et al. (2018) identified a westward deepening of SASTMW where this
155 mixes with MWs originating from the Indian Ocean. They attributed such a deepening
156 to a sinking of the core of Agulhas Rings during their crossing of the South Atlantic. This
157 echoes citetHerbette:2004 who numerically demonstrated that Agulhas Rings could subduct
158 below a front. Taking into account these works we might ask whether Agulhas Rings might
159 be an active process of MW formation as speculated by de Souza et al. (2018), and whether
160 the variations of surface properties observed in the altimetry maps are linked with lat-
161 eral mixing of waters between the eddy core and the environment, or result from a dif-
162 ferent process acting on the internal properties of eddies. Finally, by using *in situ* data,
163 numerous authors (Gordon et al., 1987; M. S. McCartney & Woodgate-Jones, 1991; Dun-
164 combe Rae et al., 1992; van Ballegooyen et al., 1994; Duncombe Rae et al., 1996; Arhan
165 et al., 1999; Garzoli et al., 1999; McDonagh et al., 1999; Schmid et al., 2003; Gladyshev
166 et al., 2008; Arhan et al., 2011; Casanova-Masjoan et al., 2017) have provided various
167 estimates of Agulhas Ring volume, heat, and salt transports. It would be interesting to
168 examine how this series of observed Agulhas Rings compare with each other and whether
169 any general information about Agulhas Rings distribution can be derived.

170 In order to provide an additional step forward in the assessment of Agulhas Ring
171 dynamics and changes across the Atlantic, we discuss here the evolution of one of these
172 eddies in the South Atlantic, sampled by a high number of vertical profiles over more
173 than a year. By making sure that the Argo profiles we used were meaningful observa-
174 tions of the eddy core, we isolated a period of the eddy lifetime during which the eddy

175 subducted below the upper-ocean layer and where thermohaline properties remained steady.
 176 During such a period of time, the eddy structure might be considered sufficiently sta-
 177 tionary to permit a meaningful reconstruction. By undertaking a comprehensive com-
 178 parison with Agulhas Ring properties discussed in the literature, we proved the robust-
 179 ness of our results and highlighted the role of specific MWs responsible for important
 180 heat and salt content anomalies with regard to the surrounding waters.

181 The paper is organized as follows. In Section 2, the data we have used are described
 182 and the methods we have developed are presented. In Section 3, the evolution of the sur-
 183 face and vertical eddy characteristics derived from satellite altimetry and Argo profiles
 184 is presented, as well as the reconstruction of the Agulhas Ring’s mean internal structure
 185 in the South Atlantic. Section 4 discusses the results we obtained in the context of pre-
 186 vious studies and assessments. A summary of the study and our conclusions about the
 187 results are provided in Section 5.

188 **3 Data and Methods**

189 **3.1 The South Atlantic Eddy Atlas**

190 We selected Agulhas Rings from the South Atlantic eddies we identified and tracked
 191 them in time with the Tracked Ocean Eddies (TOEddies) automatic detection algorithm
 192 (Laxenaire et al., 2018) applied over more than 24 years (01/1993 to 05/2017) of the “all-
 193 sat-merged” series (Duacs/AVISO+, 2015) of delayed time daily satellite altimetry maps
 194 gridded at $1/4^\circ$ in the South Atlantic and Southeast Indian oceans [70°W - 65°E ; 55°S -
 195 15°S] ((Laxenaire et al., 2018), see Figure 1a). The TOEddies method is based on the
 196 algorithm proposed and developed by Chaigneau et al. (2008, 2009) and Pegliasco et al.
 197 (2015). The eddy detection algorithm is a two-step process: it identifies the occurrences
 198 of eddies before deriving their trajectories.

199 The key assumption of eddy detection by the TOEddies algorithm is that mesoscale
 200 eddies satisfy the geostrophic balance. Therefore, the instantaneous eddy streamlines should
 201 coincide with the closed isolines of the daily Absolute Dynamic Topography (ADT) maps.
 202 First, TOEddies identifies the local extrema (maxima and minima) of ADT by compar-
 203 ing each ADT grid point to its eight neighbors as possible eddy centers in the same way
 204 that other methods defined extrema from Sea Level Anomaly (SLA) maps (e.g., Chel-
 205 ton et al., 2011; Faghmous et al., 2015). Next, it looks for the outermost closed ADT

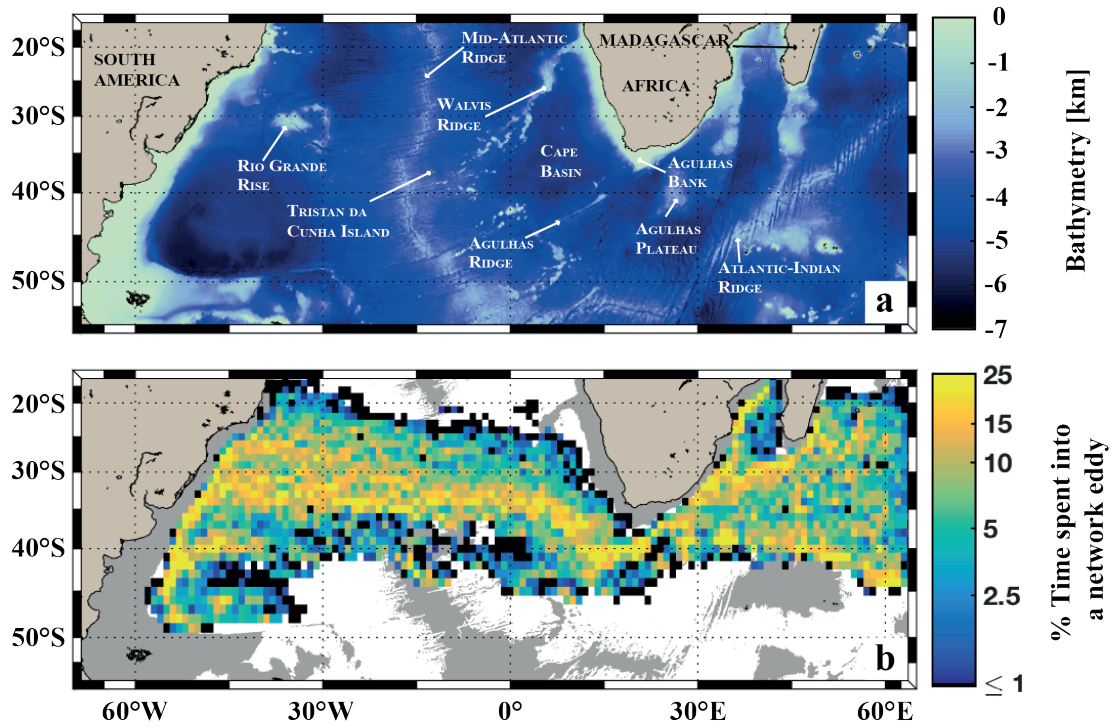


Figure 1. The study domain presented in terms of a) the local bathymetry from the ETOPO2 dataset (Smith & Sandwell, 1997) and b) the percentage of time each $2^\circ \times 2^\circ$ grid cell is occupied by the core of an eddy occurrence as part of the Agulhas Ring Eddy Network (Laxenaire et al., 2018). Figure modified from Laxenaire et al. (2018).

206 contour around each extremum. The module of the ADT difference between the extremum
 207 and this contour defines the amplitude of the detected eddy, which is considered a proxy
 208 of the eddy (surface) intensity. To filter out weak extrema we require that the extremum
 209 amplitude is greater than a threshold of 1×10^{-3} m. This value, which is small in com-
 210 parison to the precision of satellite altimetry maps, was obtained by Laxenaire et al. (2018)
 211 to improve the coherence between the TOEddies Atlas and eddies identified from sur-
 212 face drifting buoys by Lumpkin (2016). The requirement to take into account eddies as-
 213 sociated with amplitudes smaller than 1×10^{-2} m was demonstrated by Faghmous et al.
 214 (2015).

215 In addition to the outer closed ADT contour, TOEddies also identifies the contour
 216 where the azimuthal velocity of the eddy is at its maximum. This contour, associated
 217 with the gradient of the ADT, is expected to be less dependent on the hydrological struc-
 218 tures out of the eddies and easier to compare with in situ data. TOEddies uses for this
 219 purpose the geostrophic velocity derived from ADT maps and computes along each closed
 220 contour the mean azimuthal velocity $\langle V \rangle$. The contour, corresponding to $V_{max} =$
 221 $max(\langle V \rangle)$, is called the characteristic eddy contour. The area of the eddy within
 222 this contour defines what we designate as the eddy core. The mean radius, $R_{V_{max}}$, of
 223 this eddy-core area, $A_{V_{max}}$, is derived according to the following equation:

$$R_{V_{max}} = \sqrt{\frac{A_{V_{max}}}{\pi}} \quad (1)$$

224 We call this the speed radius because it is associated with V_{max} . In the same way,
 225 TOEddies defines the maximum radial extent R_{out} associated with the outer closed con-
 226 tour of the eddy. This limit is important as the eddy core defined by $R_{V_{max}}$ cannot be
 227 used alone to define either the area of influence of the eddy or the surface limiting the
 228 portion of the eddy where waters are trapped within the structure. This can be better
 229 understood by considering the ratio between the eddy azimuthal and drift speeds. This
 230 ratio is a nonlinear parameter delimiting the area of water trapped in a coherent struc-
 231 ture (Flierl, 1981; Chelton et al., 2011). For example, Agulhas Rings are characterized
 232 by a drifting speed of about $5-8 \times 10^{-2}$ m s⁻¹ (e.g., Casanova-Masjoan et al., 2017; Nen-
 233 cioli et al., 2018; Guerra et al., 2018) whereas V_{max} is of the order of several 10^{-1} m
 234 s⁻¹ (e.g., Casanova-Masjoan et al., 2017). This suggests that water outside of the limit
 235 of $R_{V_{max}}$ can be trapped within these eddies. This is confirmed by J. M. A. C. Souza

236 et al. (2011) who identified, in the South Atlantic, a horizontal extension of the eddy-
 237 trapped waters region larger than 150 km, whereas the typical $R_{V_{\max}}$ of Agulhas Rings
 238 is, in this area, 60-80 km (Guerra et al., 2018; Nencioli et al., 2018; Laxenaire et al., 2018).

239 At this stage of the TOEddies algorithm sequences, the eddy center corresponds
 240 to the local extremum of ADT, which corresponds to a defined AVISO map grid point
 241 that might not coincide with the position of the eddy center. To avoid such a constraint,
 242 TOEddies computes the centroid of the eddy-core area to determine the geometrical cen-
 243 ter of the eddy. Finally, the TOEddies algorithm computes the vortex Rossby number
 244 (Ro) that we use to quantify the (surface) eddy intensity (e.g., Chelton et al., 2011; Mkhini
 245 et al., 2014; Le Vu et al., 2018; Laxenaire et al., 2018). Ro is given by the following equa-
 246 tion:

$$Ro = \frac{V_{max}}{f \times R_{V_{max}}} \quad (2)$$

247 where f is the Coriolis parameter.

248 In order to follow the position of each detected structure, TOEddies uses an algo-
 249 rithm based on the overlapping of eddy contours at consecutive time steps (Pegliasco et
 250 al., 2015; Laxenaire et al., 2018). Using the daily AVISO fields, the method relies on the
 251 fact that mesoscale eddies move slowly (displacements of less than 10 km/day (e.g., Gar-
 252 zoli et al., 1999; Chelton et al., 2011; Laxenaire et al., 2018)) relative to their typical radii
 253 which span the range 20-200 km (Carton, 2001). Consequently, the areas occupied by
 254 an eddy for two consecutive days overlap, and this can be used to track eddies (Pegliasco
 255 et al., 2015). Laxenaire et al. (2018) determined that the optimal percentage of the eddy
 256 area overlapping between two consecutive days was equal to or larger than 50% of the
 257 smallest area among the two eddies. This parameter reduces the number of spurious iden-
 258 tifications (Laxenaire et al., 2018). If no eddy satisfies the condition of area overlapping
 259 for consecutive time steps, the research is extended for up to 5 consecutive days (i.e. half
 260 of the 10 days used by Le Vu et al. (2018)), leaving the overlapping parameter unchanged.

261 The main advantage of the TOEddies tracking method is that it also allows for tak-
 262 ing into account the merging of eddies, that is, when two or more eddies coalesce together
 263 to form one eddy, as well as the splitting of one eddy into two or more smaller eddies.
 264 Laxenaire et al. (2018) and Le Vu et al. (2018) have shown that merging and splitting

265 events strongly impact the reconstruction of eddy trajectories and lifetimes. When these
 266 events occur, the segments of trajectories are reconstructed by associating pairwise ed-
 267 dies. In the case of a splitting, a cost function (CF), modified from Pegliasco et al. (2015)
 268 and Le Vu et al. (2018) and presented in equation 3, is applied to the eddy parent and
 269 the two or more eddy descendants. The CF compares changes (Δ) in the position of the
 270 eddy center (Center), Rossby number (Ro), and radius of maximum speed ($R_{V_{\max}}$) of
 271 the eddies where $\overline{\Delta\alpha}$ and $\sigma_{\Delta\alpha}$ denote, respectively, the mean and the standard devia-
 272 tion of the differences of a variable computed from all the association of eddies either dur-
 273 ing a splitting or a merging event. The two trajectory segments that minimize CF are
 274 identified as the main trajectories whereas the remaining segments are identified as the
 275 product of the splitting and referred to higher order trajectories (Laxenaire et al., 2018).
 276 Similarly, main trajectories are identified in the case of a merging.

$$CF = \sqrt{\left(\frac{\Delta\text{Center} - \overline{\Delta\text{Center}}}{\sigma_{\Delta\text{Center}}}\right)^2 + \left(\frac{\Delta\text{Ro} - \overline{\Delta\text{Ro}}}{\sigma_{\Delta\text{Ro}}}\right)^2 + \left(\frac{\Delta R_{V_{\max}} - \overline{\Delta R_{V_{\max}}}}{\sigma_{\Delta R_{V_{\max}}}}\right)^2} \quad (3)$$

277 In this study, we consider trajectories whose lifetime is equal to or longer than one
 278 month (i.e. 4 weeks) to reduce the size of the database. This selection is reasonable in
 279 the case of Agulhas Rings that have, on average, a lifespan of a few months to several
 280 years (e.g., Byrne et al., 1995).

281 3.2 Sea Surface Temperature

282 It was shown by Lehahn et al. (2011) and J. Souza et al. (2014) that Agulhas Rings
 283 crossing the Atlantic Ocean can be associated with specific surface properties. In this
 284 framework, we will use Sea Surface Temperature (SST) data to characterize the eddies.
 285 For this purpose we retrieved the level 4 ODYSSEA SST daily database (Dash et al.,
 286 2012; Martin et al., 2012) produced by the Group for High Resolution Sea Surface Tem-
 287 perature (GHRSSST) at Ifremer/CERSAT (France). These daily cloud-free SST maps
 288 are obtained using an optimal interpolation on a global gridded at $1/10^\circ$ over the full
 289 globe merging both microwave and infrared satellite SST.

3.3 Argo profiles data and eddy colocation

While altimeter measurements are representative of the vertically integrated effect of variations in temperature and salinity over the whole water column, ADT maps do not allow for directly obtaining the vertical hydrological structure of the water column. To gain insights on this, we collocated the Agulhas Rings identified by TOEddies with *in situ* observations obtained from vertical profiles of the Argo floats international program which started in 2000. Argo floats provide a large number of CTD (Conductivity, Temperature, and Depth) vertical profiles (i.e. more than 1.5 million profiles) over the upper 2000 m of the global ocean. These data are collected and made freely available by the International Argo Program as part of the Global Ocean Observing System and the national programs that contribute to it (doi: <https://doi.org/10.17882/42182>). Argo Data Centers provide delayed mode data for each vertical profile. These data are validated and calibrated by the data assembly centers (e.g., Owens & Wong, 2009; Cabanes et al., 2016) against the most up-to-date global climatology (computed with both full depth CTD from oceanographic research cruises and validated Argo floats) to estimate errors for each Argo profile. However, because mesoscale eddies can have the ability to advect water from remote regions, the water trapped in the eddy core might have a distinct hydrological signature with respect to the surrounding climatological environment. Indeed, Argo profiles close to an eddy center significantly differ from the environment (e.g., Chaigneau et al., 2011; Pegliasco et al., 2015). Therefore, in this study, we use the Argo data downloaded from the Coriolis Global Data Center (Coriolis GDAC; <http://www.coriolis.eu.org>) that are not in the delayed mode but with control quality flags equal to 1 and 2, which refer to “good observation” and “probably good observation”.

Because data from Argo profiles are usually not recorded at constant pressure levels, we have built a homogeneous dataset by interpolating the temperature and salinity on a constant vertical grid of 10 m step. Furthermore, we applied an additional selection of Argo profiles, following Chaigneau et al. (2011) and Pegliasco et al. (2015), to ensure the consistency of the interpolation. First, we kept a profile if it contained at least one measure between the surface and 20 m and one below 1500 m. Then, we required that the vertical distance between two consecutive measurements not exceed a given threshold, depending on the depth interval. These limits are 25, 50, 75, 100, and 200 m between, respectively, the depth intervals 0-100 m, 100-300 m, 300-500 m, 500-1000 m, and be-

low 1000 m. This procedure removes about 40% of the profiles. Finally, we used the Gibbs
 SeaWater (GSW) Oceanographic Toolbox of the Thermodynamic Equation of SeaWa-
 ter TEOS-10 (McDougall & Barker, 2011) to compute the recommended hydrological
 variables, which are the conservative temperature (CT), the absolute salinity (AS), and
 the potential density anomalies referenced to the ocean surface (σ_0).

When based on the Argo system, Lebedev et al. (2007) showed that every Argo float
 moves, on average, about 4 km in 8 hours at the surface while sending 8 messages to the
 satellite. Consequently, a typical lag of 1 hour can occur between the time the Argo float
 reaches the surface and the time its position is recorded by an Argos satellite. This time
 lag may induce an error in the position of the hydrological profile of the order of 500 m,
 which is small compared to the typical radii of mesoscale eddies (Carton, 2001) as well
 as the resolution of satellite altimetry from which eddy centers and shapes are identi-
 fied. It is therefore possible to determine if a given hydrographic profile is located inside
 a detected eddy (e.g., Chaigneau et al., 2011; Pegliasco et al., 2015). The outer limit R_{out}
 is used for this determination as the trapped water in the eddy is not expected to be lim-
 ited to the $R_{V_{max}}$ contour as previously discussed.

The collocation of Argo profiles and the TOEddies eddies results in the separation
 of such profiles into three groups: those sampling a cyclonic eddy, those sampling an an-
 ticyclonic eddy, and those falling outside of either type. We define the latter as profiles
 sampling the environment within which eddies propagate. In order to quantify the hy-
 drological anomalies associated with each eddy, we computed a climatological profile char-
 acteristic of the environment outside that eddy which is then subtracted from the ver-
 tical profile sampling the core of the eddy. The climatological profile is the average of
 all the profiles measuring the environment outside the eddy. However, we require that
 their position falls within a rectangular box of $2.5^\circ \times 2.5^\circ$ centered on the eddy and
 whose dates are within a maximum temporal range of 30 calendar days (i.e. independ-
 ently of the year) from the date of the Argo profile sampling the eddy. We tested both
 the spatial and time thresholds in order to find the best fit while keeping enough pro-
 files and being sufficiently restrictive by not considering different hydrological regions
 or seasons to characterize the environment. Finally, we estimated the distance between
 each profile and the geometrical center of the eddy. This distance from the center will
 be referred as D_c in the rest of this article.

4 Results

We followed Laxenaire et al. (2018) in creating the eddy network associated with the Agulhas Ring identified in the South Atlantic Eddy Atlas. In that context, Agulhas Rings are defined as the anticyclonic eddies which are initially detected in the South-east Indian Ocean and then enter and propagate into the South Atlantic. The limit used to separate these two basins is an imaginary line connecting specific topographic structures, such as the Agulhas Ridge that defines the southeastern limit of the Cape Basin (1a). As shown by Dencausse et al. (2010), Agulhas Rings generally experience numerous mergings or splittings during their lifetime. Hence, several segments and bifurcations of trajectories have to be associated to correctly depict the whole lifespan for these eddies. In what follows, we will make use of the concept of the Agulhas Ring Eddy Network (AREN) of trajectories introduced by Laxenaire et al. (2018). This includes all the trajectories undertaken by any eddy, parent or descendant, that has merged with or split from a particular eddy or group of eddies originating in the Indian Ocean and traveling across the Indo-Atlantic limit.

The total AREN, defined during the period 1 January 2000 to 31 December 2016 (Laxenaire et al., 2018), is composed of 730 481 eddy occurrences (i.e. eddies detected in daily maps) that cluster into 6 363 trajectories. The percentage of time that each ADT grid point is inside the characteristic eddy contour of an eddy occurrence that is part of the AREN is presented in Figure 1b. The total AREN was sampled by 7 419 Argo profiles of which 826 sample Agulhas Ring main trajectories (i.e. a trajectory of an Indian anticyclone that flows into the South Atlantic basin).

Argo float No. 5902281 was identified as the one that was trapped for the longest period by a single Agulhas Ring, providing 54 vertical profiles over the period from May 2012 to November 2013, during which it propagated from Cape Basin to the Mid-Atlantic Ridge (Figure A1 in the Appendix). The long trapping of this Argo float suggests that Agulhas Rings found in this region might behave as coherent eddies, at least at 1000 m, which is the parking depth of these floats. This was also confirmed by other examples of float trapping by such eddies described in the literature. In particular, Nencioli et al. (2018) identified a comparable long trapping of an Argo float by an Agulhas Ring in this area between February 2014 and August 2015.

386 The AREN associated with the selected Agulhas Ring is presented in Figure 2. The
387 main trajectory, as defined by the cost function, is composed of segments 2, 5, and 6. The
388 network, composed of seven segments, is a general example representing the relatively
389 complex history of Agulhas Rings. It includes the various eddies and related segments
390 of trajectory that have merged with and split from this Agulhas Ring during the 4 years
391 and 7 months of its lifespan (from January 2011 to July 2015). Only the segments that
392 interact directly with the main trajectory that trapped the Argo float No. 5902281 are
393 discussed below. It is important to emphasize that, as the TOEddies Atlas could con-
394 tain some spurious eddy merging and splitting events, we manually validated the par-
395 ticular Agulhas Ring trajectory we analyze in this study by excluding eddies that ini-
396 tially merge with and then split from this trajectory during times shorter than one week.
397 The various eddies associated with this Agulhas Ring trajectory were sampled in total
398 by 112 profiles from 19 different Argo floats. The number of the profiling floats together
399 with their complete trajectories are presented in Figure A1 in the Appendix.

400 The specific Agulhas Ring trajectory network that we analyze in this study starts
401 with the shedding at the Agulhas Retroflexion of three independent Agulhas Rings. The
402 first shedding, which occurred on 8 January 2011, results in an eddy moving south and
403 entering the Cape Basin by crossing the Agulhas Ridge (dark blue, Segment 1 in Fig-
404 ure 2) and following the Southern Agulhas Rings Route defined by Dencausse et al. (2010).
405 The second and third shedding occur, respectively, in August and November 2011. The
406 second shedding gives rise to an eddy whose trajectory (mid-blue, Segment 2 in Figure 2)
407 follows the Agulhas Rings Central Route (Dencausse et al., 2010), whereas the third one
408 (light blue, Segment 3 in Figure 2) takes the Northern Agulhas Rings Route (Dencausse
409 et al., 2010). These two trajectories merge together in the eastern part of the Cape Basin
410 forming Segment 4 of the AREN (green, Figure 2). The latter merges with the South-
411 ern Route eddy (Segment 1) in the northwestern part of the Cape Basin close to the Walvis
412 Ridge. It results in Segment 5 (yellow line) that interacts with some other Agulhas Rings
413 and anticyclones along its route but without any consistent merging and splitting events
414 for 56 months until it reaches the South American Margin. There, in March 2015, it splits
415 into two eddies that move south along the American continental slope until they disap-
416 pear from the satellite altimetry field in July 2015.

417 In this study, we focus on the period of time spanning May 2012 to November 2013,
418 during which the Agulhas Ring did not merge or split while being relatively well sam-

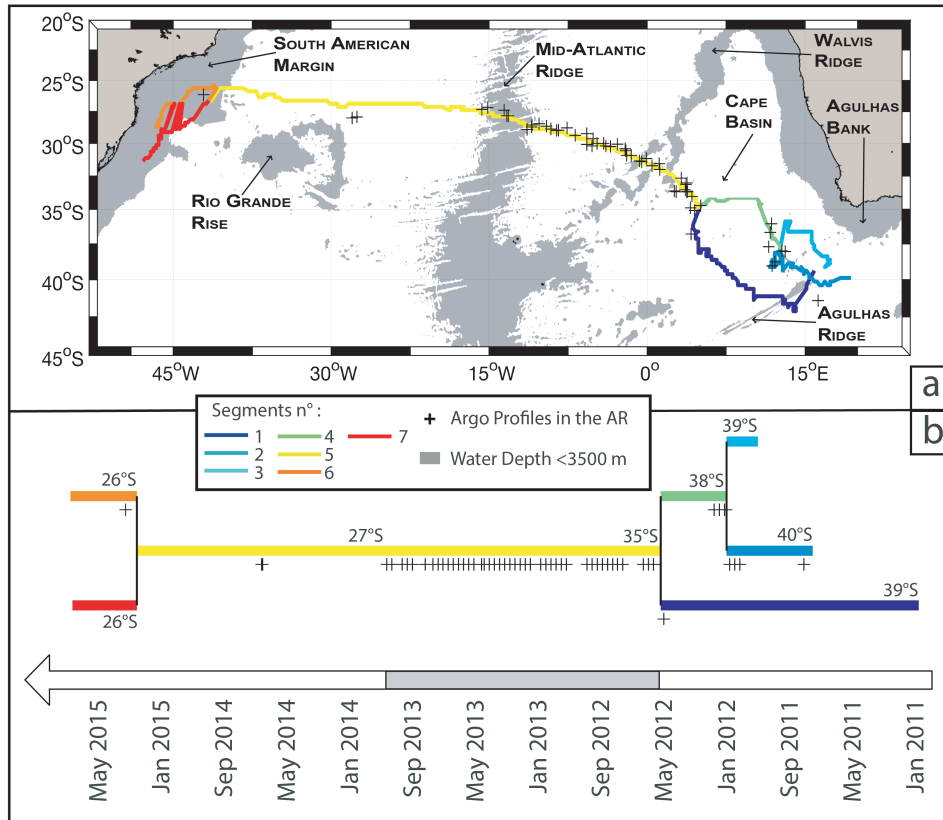


Figure 2. a) Geographical distribution of the segments (in colors) that comprise the network of trajectories for the Agulhas Ring sampled for the longest period by an Argo profiling float. The positions of the Argo profiles sampling the eddy core of the whole set of eddies that comprised this particular network are represented by the black crosses; b) A sketch displaying the various segments together with the eddy merging and splitting events and Argo profiles position as a function of time. The gray shading patches in (a) represent water depth shallower than 3500 m in the ETOPO2 dataset (Smith & Sandwell, 1997).

419 pled by multiple Argo floats (a profile sampled the structure at least every 10 days: see
 420 the black crosses in Figure 2). The dataset combines 553 days of eddy detection from
 421 ADT maps and 71 Argo vertical profiles located within the core of the eddy and achieved
 422 by 14 different Argo floats. During this period, the anticyclone associated with Segment
 423 5 leaves the Cape Basin, crossing the Walvis Ridge between October 2012 and January
 424 2013; it then propagates in the eastern part of the South Atlantic before crossing the high-
 425 est points of the Mid-Atlantic Ridge between August and October 2013 (see Figure B1
 426 in the Appendix).

427 4.1 Evolution of the Agulhas Ring surface dynamics

428 The temporal evolution of the surface signature of this Agulhas Ring (i.e. size and
 429 surface intensity) computed by TOEddies from ADT maps is presented in Figure 3. While
 430 $R_{V_{\max}}$ of this eddy is rather constant during the entire period with a median value of
 431 64 km associated with a small 8 km standard deviation (STD), R_{out} shows important
 432 variations (between 75 and 150 km and a STD of 23 km). To emphasize these differences,
 433 the evolution of the outer and characteristic contours (the latter is associated to V_{\max})
 434 is presented in Figure 4. Each contour is drawn in the translating frame of the Agulhas
 435 Ring where the position of the center of each figure corresponds to the center associated
 436 to the extrema of ADT. The contrast between the highly variable structure of the outer
 437 contour, which takes very complex shapes, and the characteristic contour, which remains
 438 coherent and keeps a relatively circular shape during the whole period of study, appears
 439 clearly. This difference might be due to the distortion of the edge of the eddy by the strain
 440 of neighbor eddies and the external flow field in general or to the small signal-to-noise
 441 ratio of the ADT outside of the eddy. In any case, we prefer to use the characteristic eddy
 442 contour and the corresponding speed radius $R_{V_{\max}}$ to estimate the size of the struc-
 443 ture, similarly to other algorithms (e.g., Nencioli et al., 2010; Duacs/AVISO+, 2017; Le Vu
 444 et al., 2018).

445 The evolution of the monthly mean V_{\max} and R_o is shown in the lower panels of
 446 Figure 3. The maximum value of V_{\max} is about $50 \times 10^{-2} \text{ m s}^{-1}$ in end of the austral
 447 fall 2012. It then decreases gradually to smaller values, below $20 \times 10^{-2} \text{ m s}^{-1}$, almost
 448 one year later. Figure 3 shows a similar decay for R_o . This is very likely due to the vari-
 449 ation of V_{\max} as the eddy size is constant and the meridional displacement is limited.
 450 One might argue that this decrease in surface intensity is related to the change of en-

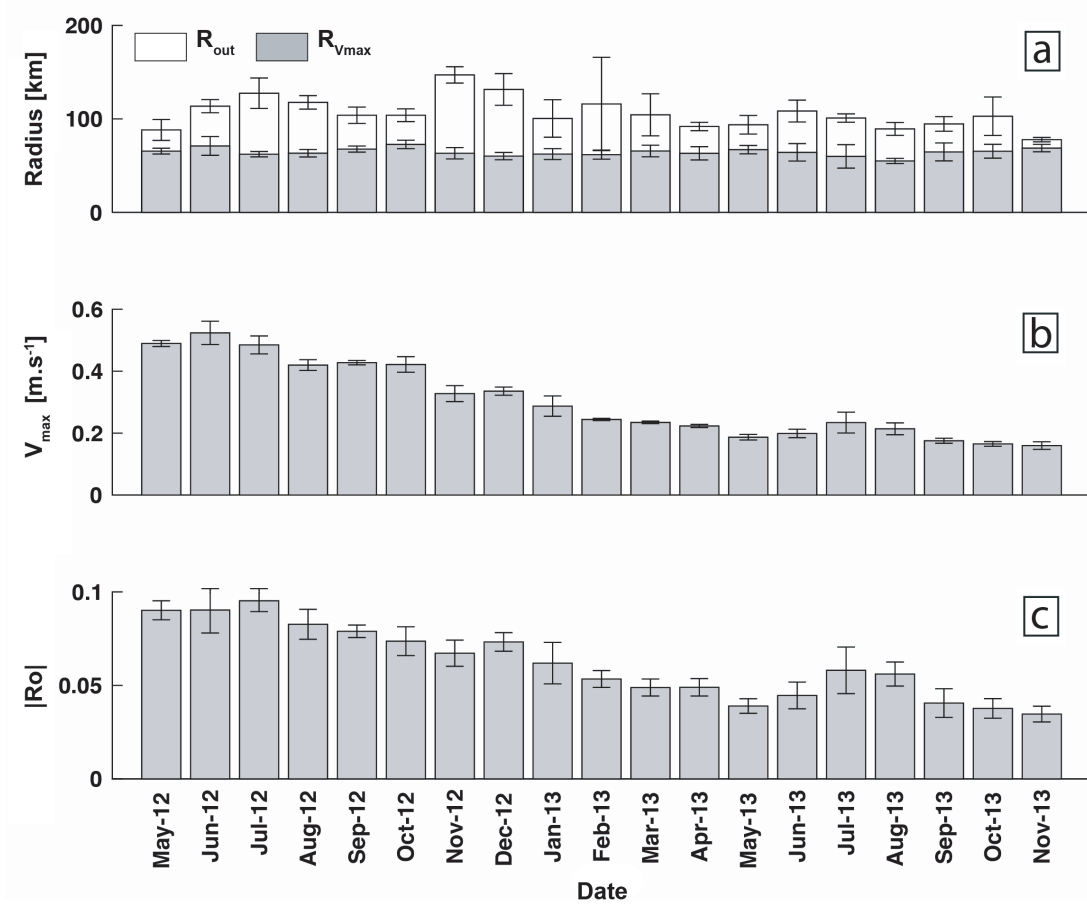


Figure 3. Temporal evolution of a) the monthly averaged equivalent radius of the outer contour (R_{out}) and the eddy-core contour where the azimuthal velocity is maximum (R_{Vmax}); b) the maximum azimuthal velocity (V_{max}); and c) the absolute Rossby number of the core ($|Ro|$) as derived from the altimetry maps. The error bars correspond to the monthly STD of these parameters.

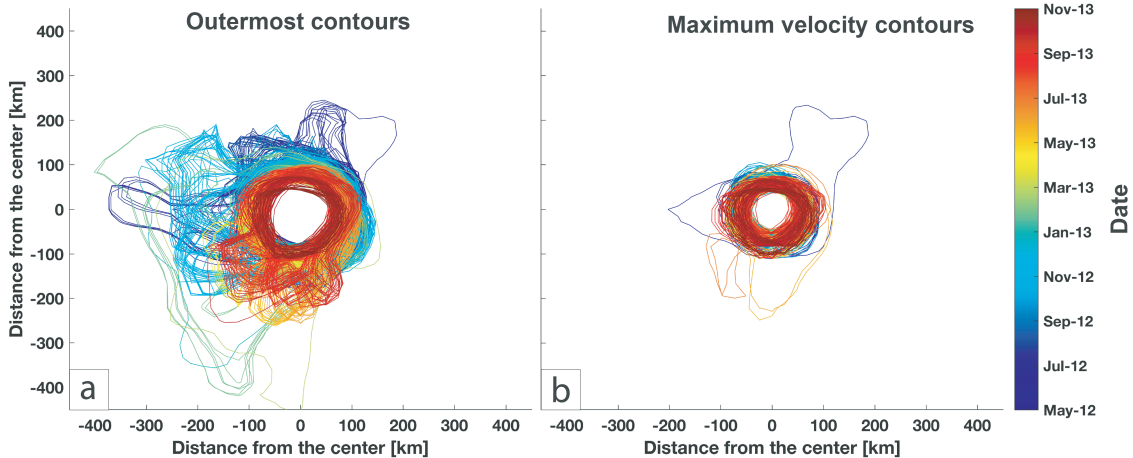


Figure 4. a) Outer contours and b) characteristic contours (associated with the maximum azimuthal speed) in the referential of the Agulhas Ring at times when an Argo float samples it.

451 vironment. However, the amplitude of the Agulhas Ring decreases from 0.4 m to 0.1 m
 452 (not shown) during its journey while the variations of the MDT interpolated at the Ag-
 453 ulhas Ring center do not exceed 0.1 m. A similar decay of surface intensity across the
 454 South Atlantic has already been documented by several authors (e.g., Byrne et al., 1995;
 455 Schouten et al., 2000; Guerra et al., 2018; Laxenaire et al., 2018). During the whole pe-
 456 riod, the Agulhas Ring absolute Ro remains small (below 0.1), which confirms that this
 457 eddy is balanced geostrophically and therefore we do not need to apply the cyclo-geostrophic
 458 correction as in Ioannou et al. (2017). A short period of intensification is visible in win-
 459 ter during July and August 2013 and a final decay of the surface signature is visible dur-
 460 ing the two last months of the period under study.

461 4.2 Evolution of the internal structure

462 In order to estimate the evolution of the conservative temperature (CT), absolute
 463 salinity (AS) and potential density (σ_0) inside the Agulhas Ring, we first divided the time
 464 period into 10-day intervals. For each of these 10-day intervals we selected the Argo pro-
 465 files closest to the eddy center. The selected vertical profiles are presented in the left pan-
 466 els (a, c, and e) of Figure 5 and the associated anomalies, computed as the difference be-
 467 tween the vertical profiles sampling the eddy and the mean environmental profiles, are

468 presented in the right panels (b, d, and f) of the same Figure together with the distance
469 (Dc) of the Argo profile from the eddy center.

470 The climatologic profiles used to compute the anomalies as well as the number of
471 profiles used to compute the first 1500 m of each climatological profile at each time step
472 are presented in Figure 6. For this study we selected only Argo profiles associated with
473 a maximum depth of over 1500 m. Indeed, the number of profiles sampling the upper
474 layer of the water column is higher than those reaching depths of over 1500 m. The min-
475 imum available profiles within the eddy core close to the surface is 40, but this decreases
476 to 28 for profiles reaching a depth of 1800 m (not shown). The maximum number of pro-
477 files is 118 for the upper 1500 m of depth, and 93 for profiles reaching 1800 m (not shown).
478 In the climatological profiles, the upper 200 meters appear as the most variable. A sur-
479 face layer of low density appears in October 2012 concomitant to the onset of the sum-
480 mer seasonal stratification as well as the drifting of the eddy into warmer waters. This
481 limit, characterized by the isopycnal 26.2 kg m^{-3} , appears to continuously thicken dur-
482 ing a period of more than a full year. The layers below this isopycnal show more steady
483 characteristics during the full period, albeit a relatively small downlift of the isolines ap-
484 pears between a depth of 200 and 400 m and an uplift appears below 400 m. Very likely,
485 this is due to the westward thinning of the Antarctic Intermediate Water (AAIW) layer
486 marked by a minimum of salinity around 1000 m as discussed by Rusciano et al. (2012).

487 Figure 5 presents the hydrological characteristics of the Agulhas Ring as provided
488 by the Argo profiles sampling the eddy. It shows that important variations in the eddy
489 properties occur in the upper 200 m. Here, a shallow and low-density layer (limited by
490 the 26 kg m^{-3} isopycnal) is visible in May 2012 (during the end of the austral fall). This
491 layer is eroded at the beginning of the austral winter (from June 2012) and reappears
492 in October 2012 during the austral spring. This layer might be associated with the sea-
493 sonal cycle, with the formation and erosion of a seasonal thermocline. However, simi-
494 larly to the behavior shown by the climatological profiles (Figure 6), this layer contin-
495 ues to thicken from October 2012 to November 2013, not showing any further winter ero-
496 sion. This suggests that the upper eddy layer not only evolves with the seasonal cycle
497 but is also affected by the displacement of the eddy into a different hydrological region
498 (the South Atlantic subtropical gyre) characterized by a shallow permanent stratifica-
499 tion.

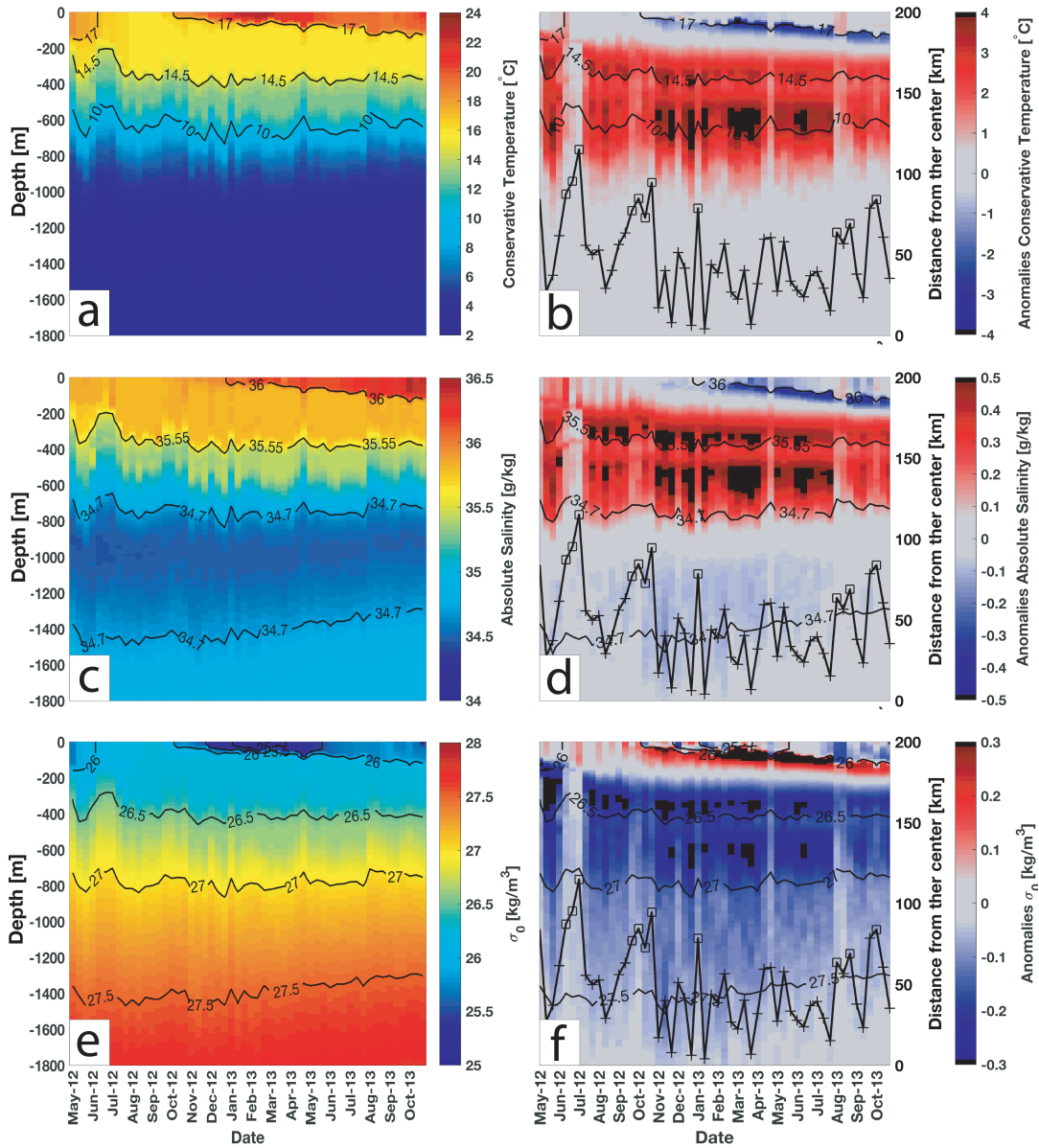


Figure 5. a) Conservative temperature, b) conservative temperature anomaly, c) absolute salinity, d) absolute salinity anomaly, e) potential density, and f) potential density anomaly for the closest Argo profiles to the Agulhas Ring center for each 10-day interval as a function of time and depth. Black lines with markers in each right panel represent the distance of each profile from the eddy center (D_c) whose scale is presented on the y-axis on the right of panels b, d and f. The marker is a cross for profiles inside the characteristic contours; otherwise it is indicated as a square. Selected isotherm, isohaline, and isopycnal levels are added to the corresponding panels for both the full fields and the anomalies.

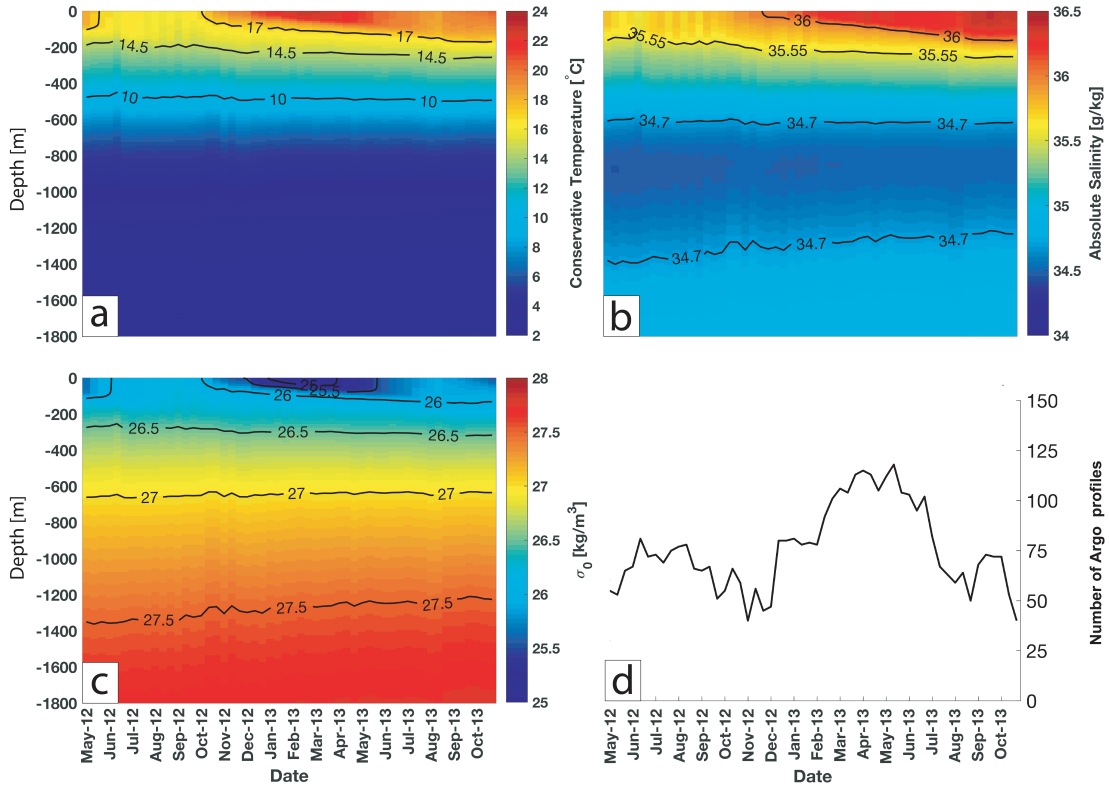


Figure 6. a) Conservative temperature, b) absolute salinity, and c) σ_0 for the environment climatological profiles we used to compute the Agulhas Ring vertical property anomalies in Figure 5; d) Number of averaged Argo profiles used to to compute the first 1500 m of the environment climatology.

500 The Argo data also show a relatively high correlation between vertical properties
 501 and the distance (Dc) of the profile from the eddy center (see, for instance, the varia-
 502 tions of Dc together with those of the isolines 10°C, 34.7 g kg⁻¹, and 27 kg m⁻³ in Fig-
 503 ure 5a,d,e). As expected for a warm and salty core anticyclone such as an Agulhas Ring,
 504 the isolines are deeper near the center of the structure than at its edges. The correla-
 505 tion among the eddy hydrological properties and Dc is particularly evident from the ver-
 506 tical CT, AS, and σ_0 anomalies (Figure 5b,d and f). Their amplitude variations are in-
 507 deed intimately linked with Dc variability and this through the whole water column. In
 508 particular, Figure 5b,d and f show clearly a strong reduction in the anomaly amplitude
 509 when Dc is larger than 65 km. This corresponds to the periods June-July 2012, Octo-
 510 ber 2012, January 2013 and, later on, in August and October 2013.

511 The eddy property anomalies (Figure 5b,d and f) show that the Agulhas Ring is
 512 warmer, saltier and less dense than the environment. A marked positive anomaly in AS
 513 (> 0.2 g kg⁻¹) and CT ($> 1^\circ\text{C}$) down to at least 800 m appears clearly for small Dc (Dc
 514 < 50 km). Moreover, these anomalies exhibit a striking vertical pattern characterized,
 515 from November 2012 to August 2013, by two well-separated extrema roughly located at
 516 a depth of -350 m and -650 m. Such a vertical structure strongly suggests the presence
 517 within the eddy of two cores of water masses very different from the environment. It should
 518 be noted here that σ_0 anomaly for the two distinct water-mass cores is about -0.3 kg m⁻³,
 519 a value six times higher than the STD of the environment σ_0 (0.05 kg m⁻³ (not shown)).
 520 It is worth noting that, after November 2012, negative anomalies of AS are found within
 521 the eddy below 1000 m.

522 To better understand the vertical structure of the Agulhas Ring, we plotted the
 523 Brunt Väisälä frequency squared N^2 in the Argo profiles plotted in Figure 5, and the cli-
 524 matological environment in Figure 7. N^2 is computed from equation 4, where g is the
 525 gravitational acceleration and ρ_0 the density of reference set to 1000 kg m⁻³.

$$N^2 = \frac{-g}{\rho_0} \frac{\partial \rho}{\partial z} \quad (4)$$

526 The environment profiles exhibit a seasonal cycle characterized by the development
 527 of a winter mixed layer (low values of N^2 , below 1×10^{-5} s⁻²) extending, on average, to
 528 a depth of 150 m in August-September (Figure 7b). On the other hand, the eddy core
 529 is characterized by a considerably deeper mixed layer which develops during the first five

548 lies to discriminate surface and subsurface intensified eddies. Indeed, anticyclonic eddies
 549 are associated with positive Sea Level Anomalies. If they are surface eddies, they are ex-
 550 pected to correspond to positive SST anomalies, whereas if they are subsurface eddies,
 551 they should be associated with negative SST anomalies as a consequence of the doming
 552 of the isotherm above their hydrological core.

553 For this purpose, we used the ODYSSEA SST dataset (Dash et al., 2012; Martin
 554 et al., 2012) that we have interpolated at the position of the eddy center during the pe-
 555 riod of interest (see Figure 8). For each date, we computed the average of the SST field
 556 for all the points in the square box area of $300\text{ km} \times 300\text{ km}$ centered on the eddy cen-
 557 ter (i.e. 150 km corresponds to the maximum R_{out}). The anomalies are computed by
 558 subtracting this mean SST from the SST value at the center of the eddy. These anoma-
 559 lies are presented in Figure 8. It appears from this figure that they change sign between
 560 September and October 2012. This is in accordance with what we identified as the be-
 561 ginning of the isolation of the Agulhas Ring from the ocean surface, as previously dis-
 562 cussed in the analysis of Figures 5 and 7. Such a change of sign can be due to the mod-
 563 ification of the background environment while the eddy moves into subtropical waters.
 564 Yet, the absolute SST (blue line in Figure 8) clearly shows a seasonal cycle as well as
 565 an interannual increase, indicating that variations also occurred within the eddy. It is
 566 not consistent with a fixed patch of constant temperature drifting into another environ-
 567 ment. However, J. Souza et al. (2014) discussed the presence of negative SST anoma-
 568 lies in relation to Agulhas Rings still connected with the ocean surface. They explained
 569 this by a modification of the Ekman pumping due to the presence of the eddy and that
 570 it may induce dipole SST anomalies with the center of an Agulhas Ring associated to
 571 a negative SST anomaly, whereas a positive anomaly would correspond to the eddy bound-
 572 aries.

573 To assess the geographical pattern of SST anomalies, we computed monthly SST
 574 anomaly maps in the moving frame of the Agulhas Ring. They are presented in Figure C1
 575 in the Appendix. These maps show that, in July 2012, the Agulhas Ring core is asso-
 576 ciated with positive SST anomaly values. These, however, are lower within the eddy's
 577 inner core than at its boundaries, which might confirm the conclusions of J. Souza et al.
 578 (2014). However, after October 2012, the date we identified as that corresponding to the
 579 isolation of the main hydrological core of the Agulhas Ring from the ocean surface, the
 580 SST dipole-like anomaly disappears and the Agulhas Ring becomes associated with a

581 strong patch of negative SST anomalies, confirming the subsurface nature of the eddy
 582 following criteria of Assassi et al. (2016) and (Schütte et al., 2016). Positive anomalies
 583 still exist close to the eddy boundary but are localized at the eddy western side, a fea-
 584 ture that can be explained by the stirring of the environment due to the anticlockwise
 585 rotation of the Agulhas Ring in the presence of a north-south gradient of temperature.

586 The results we obtained by analyzing two independent datasets (Argo vertical pro-
 587 files and satellite SST) corroborate the finding that the main hydrological core of the Ag-
 588 ulhas Ring, initially connected to the surface, subducted into the ocean interior while
 589 leaving the Cape Basin and penetrating into the South Atlantic subtropical gyre. We
 590 follow here Williams (2001)’s definition of subduction as the transfer of fluid from the
 591 mixed layer to the stratified thermocline (i.e. below the seasonal mixed layer). It is clear
 592 that the winter mixed layer developing between March 2013 and September 2013 stays
 593 separated from the shallower eddy core of homogeneous water. However, it is difficult
 594 to select the main process generating the observed subduction. Indeed, the observed be-
 595 havior might result from a modification of the eddy upper-layer waters by ocean-atmosphere
 596 interactions Arhan et al. (2011) as well as by the lateral penetration of an eddy below
 597 the lighter upper water of the South Atlantic subtropical gyre.

598 In order to gain insight into this question, we evaluated (Figure D1 in the Appendix)
 599 the differences in terms of T-S properties for Argo profiles sampling segment 5 during
 600 the period November 2012 to November 2013 near the eddy center ($D_c < 25$ km, in red
 601 in Figure D1) and those close to the eddy boundaries ($150 < D_c < 200$ km, in blue in
 602 Figure D1). This analysis shows that the upper-layer eddy water masses are different
 603 to those of the environment. However, the eddy upper-water velocities still verify the eddy-
 604 coherent condition defined by Flierl (1981) and used in many studies since then [(e.g.,
 605 Chelton et al., 2011): the minimum of V_{\max} is larger than 0.2 m^{-1} (see Figure 3) while
 606 the drifting speed of the eddy does not exceed 0.1 m s^{-1} . This suggests that the observed
 607 subduction could result from the surface modification of the Agulhas Ring advected wa-
 608 ter. Using a very high-resolution numerical simulation in the Cape Basin, Capuano et
 609 al. (2018) showed that submesoscale instabilities (of different type) determine, in win-
 610 ter, the formation of deep mixing layers in Agulhas Rings and, in summer, induce an in-
 611 tense upper-layer restratification. As the Agulhas Ring moves westward exiting the Cape
 612 Basin, it enters a region of milder air-sea interactions that are not sufficiently strong to



Figure 8. Sea Surface Temperature (blue) and associated anomalies (red) interpolated from the ODYSSEA SST dataset (Dash et al., 2012; Martin et al., 2012) at the center of the Agulhas Ring. The anomalies are computed by subtracting the mean SST (computed as the average of the SST in the square box area of $300\text{ km} \times 300\text{ km}$ centered on the eddy center) to the SST value in the center of the eddy. All the data were smoothed by a moving average associated with a monthly window.

613 erode the upper-layer stratification. Such a process might explain the isolation of the Ag-
 614 gulhas Ring subsurface core from the ocean surface.

615 Figure 7 reveals the presence, between October 2012 and August 2013, of a sec-
 616 ond, albeit thinner, homogeneous layer located deeper than the first one (between 500
 617 and 600 m). It corresponds to the second thermohaline anomalies core that appears in
 618 the Argo vertical profiles sampling the Agulhas Ring (Figure 5). After August 2013, the
 619 Argo profiles sample the eddy farthest from the eddy center. This prevents any conclu-
 620 sion as to what makes this deeper core of MW disappear. Indeed, on August 2013, the
 621 eddy is located over the Mid-Atlantic Ridge (see Figure B1). We suggest that the inter-
 622 action between the eddy and the topography caused an intense mixing at depth with neigh-
 623 boring waters. Or, it might be that, because of the larger distance of the sampled pro-
 624 files from the eddy center after August 2013, this core of MW that was probably small
 625 in its lateral extent was not sampled by the Argo floats.

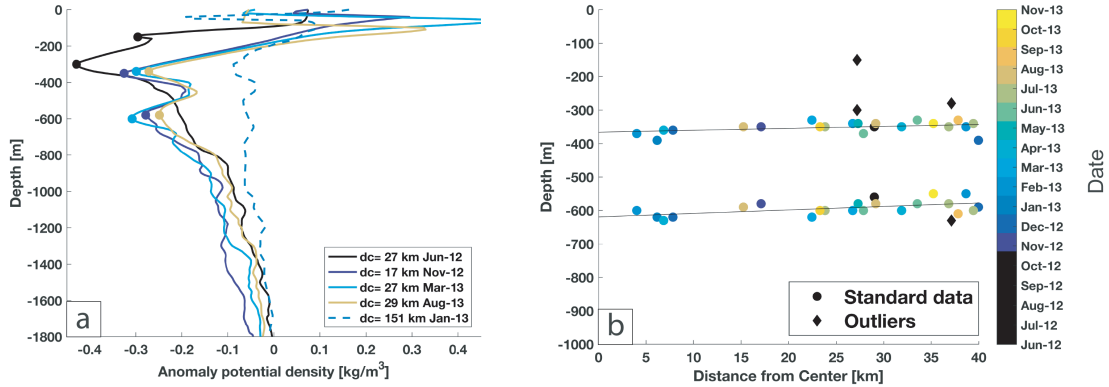


Figure 9. a) Argo vertical profiles of density anomaly. Four lie close to the eddy center and show the two mode waters' thermohaline extrema (solid lines); one is located farther away (dashed lines) and does not display these two mode waters' related extrema. b) Depth of the two mode water cores as a function of D_c for all the profiles lying at less than 40 km from the eddy center. An outlier is identified if both extrema in a profile are at a distance from the black lines greater than the STD associated with the determination of each extremum.

626 To prevent the interference of the varying position of Argo floats while attempt-
 627 ing to determine the eddy evolution in time, we select, in the following section, only those
 628 Argo profiles located within the eddy core (i.e., $D_c < R_{V_{\max}}$). The density anomalies
 629 associated with four profiles separated by four or five months between June 2012 and
 630 August 2013 are shown as solid lines in Figure 9a. All these profiles are located inside
 631 the eddy and close to its center ($15 \text{ km} < D_c < 30 \text{ km}$), albeit it is worth mentioning
 632 that accuracy in determining the eddy center from ADT maps is limited and this might
 633 induce significant errors in D_c estimates. For comparison, Figure 9a presents, in a dashed
 634 line, a vertical profile undertaken in January 2013 by an Argo float far from the eddy
 635 center ($D_c = 151 \text{ km}$). From this figure, it appears clearly that this profile does not sam-
 636 ple any of the eddy MW cores.

637 Figure 9b shows the depth of the two Agulhas Ring MW cores as a function of D_c
 638 computed by taking a large number of Argo profiles, all located near the eddy center (D_c
 639 $< 40 \text{ km}$) and defined as the vertical maxima of thermohaline anomalies. The vertical
 640 location of the two thermohaline anomaly maxima varies weakly with time and with the
 641 distance of the Argo profile from the eddy center. We also computed the STD of the resid-
 642 ual between each extremum and the linear regression obtained between D_c and the depth

643 of the two anomaly peaks. We considered as outliers those profiles whose residuals are
 644 larger than the STD (Figure 9b). From this, it appears that two of the three profiles
 645 that sampled the eddy before it subsided below the surface in November 2012 differ sig-
 646 nificantly from the others. For the latter, the density anomaly of the core seems to keep
 647 roughly the same depth for several months.

648 **4.3 Reconstruction of the subsurface structure of an Agulhas Ring**

649 Figures 5 and 7 show that, from November 2012 to November 2013, the upper 150
 650 m layer of water within the Agulhas Ring limits was characterized by a strong seasonal
 651 variability, whereas below it, the thermohaline properties underwent only small varia-
 652 tions. We therefore assumed, as a first-order approximation, that the Agulhas Ring be-
 653 low a depth of 150-200 m was in a quasi-steady state, and that the upper 150 m layer
 654 of water no longer belonged to the eddy main hydrological core.

655 Similarly to the assumptions of J. M. A. C. Souza et al. (2011) and Nencioli et al.
 656 (2018), we also hypothesized that the eddy had a quasi-circular symmetry. The ampli-
 657 tude of the subsurface anomaly will then depend only on the distance (D_c) between the
 658 Argo float position and the geometrical eddy center. As discussed previously, $R_{V_{\max}}$
 659 can be considered to be constant during at least the period November 2012 to Novem-
 660 ber 2013 (with a median and mean radius of 63 km and a STD of 8 km). However, to
 661 test the validity of a quasi-circular eddy assumption, we estimated the ellipticity (ϵ) of
 662 the characteristic eddy contours derived from the daily ADT maps, from equation 5 where
 663 a is the semi-major and b the semi-minor axis.

$$\epsilon = 1 - \frac{b}{a} \quad (5)$$

664 The ellipticity remains small from November 2012 to November 2013, with a me-
 665 dian value of 0.11, a mean of 0.12 and a STD of 0.07. We therefore restricted our anal-
 666 ysis to this 12-month period to ensure the validity of the axisymmetry hypothesis for the
 667 eddy, which would otherwise not be valid for large ellipticity values.

668 In order to reconstruct the Agulhas Ring axisymmetric structure, we used 71 Argo
 669 profiles that were located within a distance of 185 km (i.e. $\sim 3 \times R_{V_{\max}}$) from the geo-
 670 metrical eddy center (Figure 10) during the November 2012 to November 2013 period.

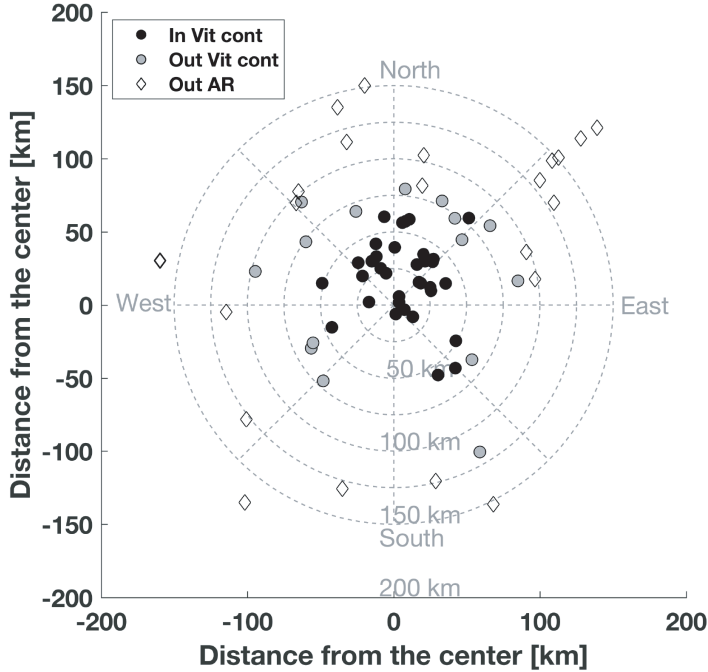


Figure 10. Position of the Argo profiles in the moving frame of the Agulhas Ring. The center of the frame corresponds to the centroid of the characteristic eddy contour delimited by $R_{V_{\max}}$ and computed from ADT maps. The filled circles indicate Argo profiles inside the characteristic eddy contour, the gray circles those inside outer eddy edge, and the empty diamond those outside the Agulhas Ring and any other neighboring eddy and lying at a 160 km radius from the Agulhas Ring center.

671 The Argo float No. 5902281 sampled more than 54% of the profiles, whereas other floats
 672 surfaced sporadically inside the eddy. Overall, during the given 12-month period, the Ag-
 673 ulhas Ring was sampled by 52 profiles within a distance of 100 km from the eddy cen-
 674 ter.

675 Different techniques have been used in the literature to attempt a reconstruction
 676 of the vertical structure of mesoscale eddies from sparse *in situ* observations. Most of
 677 them employed a composite eddy reconstruction approach (e.g., Schütte et al., 2016; Amores
 678 et al., 2017), while others tried to recover the structure of specific eddies. For example,
 679 Chaigneau et al. (2011) objectively mapped observations onto a 10-km grid assuming
 680 an isotropic Gaussian covariance decorrelation scale of 100 km, and J. M. A. C. Souza
 681 et al. (2011) fitted to a 7th order one-dimensional Lagrange polynomial. However, the

682 Gaussian method smooths out horizontal gradients, whereas high-order polynomials of-
 683 ten induce an overshooting of the hydrological variables at the outer edge of the recon-
 684 structed eddies. To avoid these drawbacks, we used a generic function tending towards
 685 zero outside the eddy.

686 The generic function we used to fit the (CT, AS) anomalies we defined previously
 687 at each depth (see equation 6) is that of an α -Gaussian vortex (see for example Carton,
 688 2001; Le Vu et al., 2018; Zeitlin, 2018). The parity of this generic function ensures the
 689 axisymmetry of the reconstructed eddy and an exponential reduction in its anomalies
 690 far from the center. The $A_0(z)$ profile represents the maximal core anomaly inside the
 691 eddy. To suggest a first guess for $A_0(z)$, we use the mean of the three Argo profiles clos-
 692 est to the eddy center while the parameters α and $R_0(z)$ are set initially to 2 (i.e. a purely
 693 Gaussian shape as used by Nencioli et al. (2018)) and $R_{V_{\max}} = 63$ km respectively. Then,
 694 the three parameters (A_0 , R_0 and α) associated with the generic function 6 are adjusted
 695 at each depth level, minimizing the residuals between the fitting of the equation and the
 696 observations using the Trust Region Reflective algorithm (Branch et al., 1999) with the
 697 function `lsqcurvefit` of the MATLAB Library. As we expect the anomalies to increase
 698 toward the center, we do not allow A_0 to be lower than the first guess which ensure to
 699 preserve the large scale gradient. Moreover, it is worth noting that the Trust Region Re-
 700 flective algorithm can stop at local best fit thus several adjustments are run at each lev-
 701 els varying the initial guess of α and $R_0(z)$ to detect the global best fit. Below 200 m,
 702 the values obtained for the various parameters by fitting the function 6 are between 1.9
 703 and 2 with a STD between 0.05 and 0.15 depending of the variable. Similarly, mean R_0
 704 is between 66 and 76 km with a STD ranging between 10 and 17 km.

$$Anom(r, z) = A_0(z) e^{-\frac{1}{\alpha} \left(\frac{r}{R_0(z)} \right)^\alpha} \quad (6)$$

705 Finally, to obtain a first estimation of the thermohaline structure of the Agulhas
 706 Ring ($Anom(r, z)$), we added the average of all the profiles of the environment computed
 707 for each vertical level to the reconstructed anomalies.

708 Figure 11 shows the isolines of CT, AS, and σ_0 for the reconstructed Agulhas Ring
 709 (defined with the acronym RecAR from here on), superimposed over the raw Argo pro-
 710 file data plotted as a function of Dc. A more detailed examination of the σ_0 reconstruc-

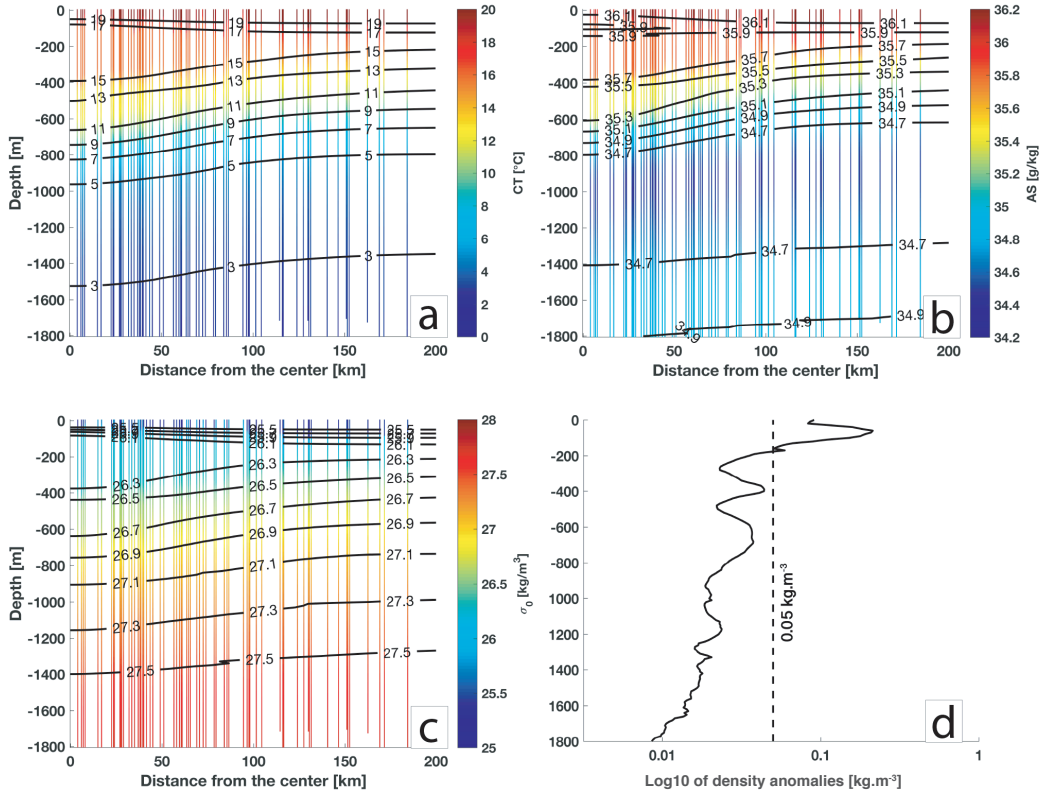


Figure 11. Superposition of the observed (background color) and the reconstructed (black contours) Agulhas Ring of the a) conservative temperature, b) absolute salinity, c) σ_0 , and d) root-mean-square error between the observed σ_0 anomalies and the reconstructed values computed at each depth.

711 tion is shown in Figure E1 in the Appendix. Both figures show, below the surface, a par-
 712 ticularly good agreement between the isocontours of RecAR and the raw Argo data.

713 Figure 11 shows clearly two layers of homogeneous thermohaline properties. A first
 714 one is centered around a depth of 250 m, between the isolines $17^{\circ}\text{C} - 15^{\circ}\text{C}$, 35.9 g kg^{-1}
 715 $- 35.7 \text{ g kg}^{-1}$, and $26.1 \text{ kg m}^{-3} - 26.3 \text{ kg m}^{-3}$. The maximal thickness of this layer is
 716 ~ 350 m at the eddy center. The second homogeneous layer is centered at a depth of 500
 717 m, and it is characterized by the isoline intervals $13^{\circ}\text{C} - 11^{\circ}\text{C}$, $35.5 \text{ g kg}^{-1} - 35.3 \text{ g kg}^{-1}$,
 718 and $26.5 \text{ kg m}^{-3} - 26.7 \text{ kg m}^{-3}$. One can observe that the depths of these cores do not
 719 correspond to those obtained from anomalies in Figure 9 but correspond well with the
 720 position of the N^2 cores at the end of the time series in Figure 7. Our impression is that
 721 the position of the maximum anomaly shows the depths of the bottom of each layer of
 722 MW just above the compensation that occurs below each MW. Consequently, the anoma-
 723 lies cannot be used to identify the center of a hydrological core.

724 In order to test the accuracy of the three-dimensional reconstruction, we computed
 725 the root mean square (RMSE) of the difference between the *in situ* measurements pro-
 726 vided by every Argo profile and RecAR (Figure 11d). The values of RMSE vary between
 727 0.01 and 0.05 kg m^{-3} , which is six times less than the maximum σ_0 anomalies. This gives
 728 us confidence in the eddy properties reconstruction.

729 The two local maxima at depths of 400 and 700 m in Figure 11 correspond to the
 730 region of strong variation of properties when moving from the eddy center outward along
 731 an constant line of depth. However, near the surface the errors are considerably larger.
 732 The RMSE value of 0.05 kg m^{-3} lies between a depth of 150 and 160 m whereas the largest
 733 RMSE value (0.2 kg m^{-3}) is found at 60 m. At these depths waters undergo a strong
 734 seasonal forcing and therefore we cannot consider that the thermohaline properties of
 735 the eddy remain constant here for the whole year. As discussed previously, the Agulhas
 736 Ring has subducted below the subtropical gyre upper 150 m of warm waters. Hence, we
 737 assume that the eddy upper limit is below this layer. We choose as such a limit for Re-
 738 cAR a specific isopycnal - the 26.2 kg m^{-3} isopycnal - which corresponds to the specific
 739 limit identified in Figure 5 as the separation between the part of the water column that
 740 evolves over time and the one which is steady below it, rather than a fixed depth. It is
 741 important to note here that the depth of this isopycnal varies between 150 m near the

742 eddy center and 170 m away from it. In what follows, we will consider as RecAR the wa-
 743 ters lying below the 26.2 kg m^{-3} isopycnal surface.

744 By using RecAR as the reference, we computed the error associated with the val-
 745 ues of D_c obtained in collocating the Argo profiles with the eddy as detected by the TOEd-
 746 dies algorithm. A distance is computed between each observation on the σ_0 levels, be-
 747 tween a depth of 200 m and 1000 m, from the Argo profiles and the corresponding value
 748 in the RecAR. This corresponds to the distance between each observation and the Re-
 749 cAR isoline taken at the same depth as shown in Figure E1 in the Appendix. The lower-
 750 limit depth of 1000 m was fixed as the horizontal gradient of σ_0 is weak below this depth.
 751 This would have impacted the accuracy in the determination of D_c . From the 66 pro-
 752 files, we computed mean values of this distance equal to 16 km associated with a STD
 753 of 8 km.

754 Figure 12 shows the CT, AS, and σ_0 anomalies of RecAR as well as the Brunt Väisälä
 755 frequency squared (N^2). Such reconstruction clearly shows a dual core structure for Re-
 756 cAR. This is particularly discernible from the two low stratification layers in Figure 12d.
 757 The anomalies are important as they materialize the eddy content and transport of proper-
 758 ties, such as heat and salt. The upper core lies at 350 m with peak anomalies of 3.7°C ,
 759 0.56 g kg^{-1} , and -0.35 kg m^{-3} for, respectively, conservative temperature, absolute salin-
 760 ity and potential density. The lower core lies at a depth of around 550 m and is char-
 761 acterized by anomalies of 4.4°C , 0.62 g kg^{-1} , and -0.31 kg m^{-3} . The anomalies of con-
 762 servative temperature and absolute salinity are more intense within the lower core but,
 763 due to their inverse effect on density, the density anomalies are nearly equal for both cores.

764 In order to estimate the three-dimensional velocity structure (i.e. $V(r, z)$) for Re-
 765 cAR we use the non-linear thermal wind equation 7 (e.g., Ioannou et al., 2017):

$$\frac{1}{r} \frac{\partial V^2}{\partial z} + f \frac{\partial V}{\partial z} = \frac{-g}{\rho_0} \frac{\partial \rho}{\partial r} \quad (7)$$

766 To solve this partial differential equation, the velocity field is set to 0 at a depth
 767 of 1800 m (i.e. $V(r, z = -1800) = 0$). The resulting velocity field is shown in Figure 13a.
 768 The maximum value of the azimuthal velocity is equal to $31 \times 10^{-2} \text{ m s}^{-1}$. It is located
 769 at a depth of 200 m and at a distance of 63 km from the eddy center. This value is very
 770 close to the mean maximum speed radius, $R_{V_{\max}} = 64 \text{ km}$, estimated from the surface

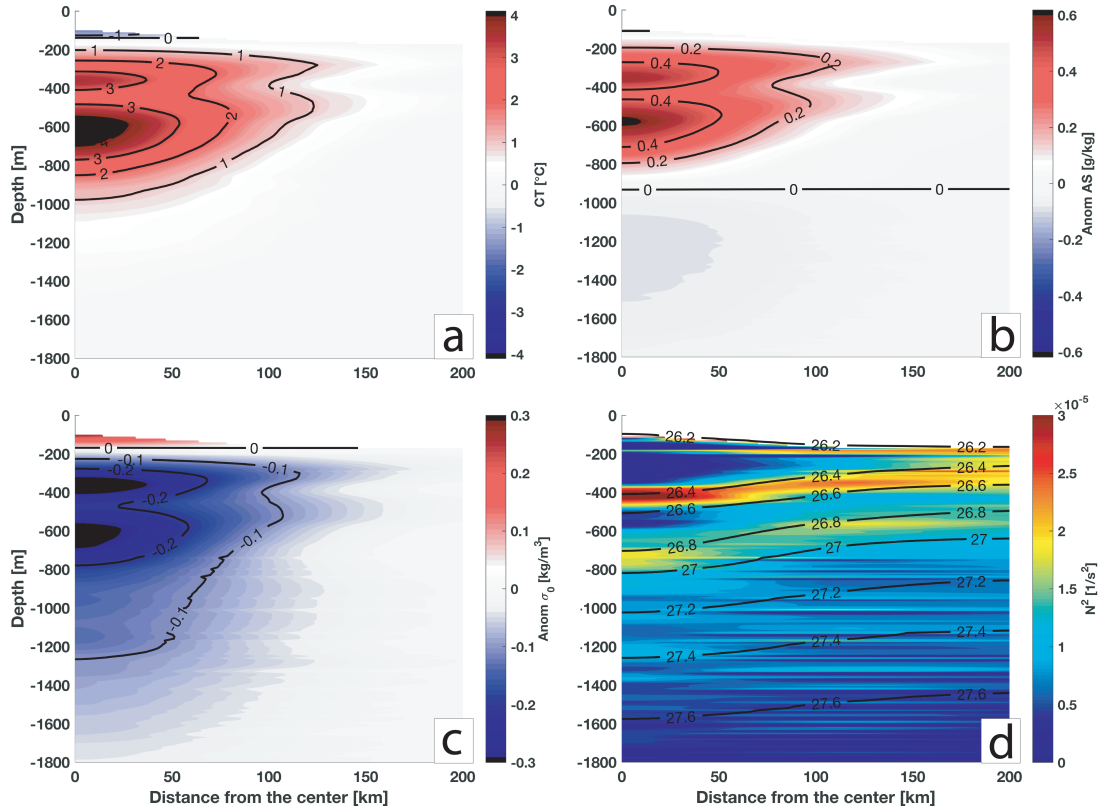


Figure 12. Anomalies of a) conservative temperature, b) absolute salinity, c) σ_0 , and d) Brunt Väisälä frequency squared (N^2) for the reconstructed Agulhas Ring. Contours in d) are isopycnals of the reconstructed Agulhas Ring. The gray patch near the surface in each panel corresponds to the region above the isopycnal surface 26.2 kg m^{-3} , which marks the separation between the subtropical gyre upper warm waters and the eddy upper limit.

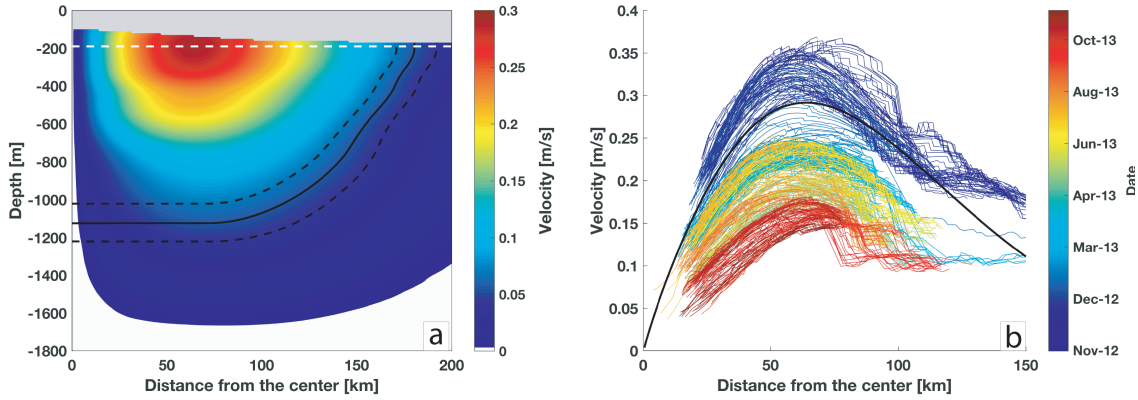


Figure 13. a) Velocity field of the reconstructed Agulhas Ring computed from hydrographic data and b) evolution of the geostrophic currents derived from satellite altimetry maps as a function of the distance from the center. The black line in b) is the velocity derived from hydrographic data at -200 m (i.e. where this velocity is at its maximum). A dashed white line is added at this depth in panel a). The black line in panel a) corresponds to the separatrix where the velocity is equal to $5.7 \times 10^{-2} \text{ m s}^{-1}$ which is the median translation speed during the period November 2012 to November 2013. The dashed lines indicate the \pm one STD ($\pm 1.4 \times 10^{-2} \text{ m s}^{-1}$) limits of the separatrix. The gray patch in panel a) corresponds to the region above the isopycnal surface 26.2 kg m^{-3} , which marks the separation between the upper subtropical gyre waters and the upper limit of the eddy.

771 geostrophic velocity field during the 12-month period. In comparison to the grid res-
 772 olution of ADT maps ($1/4^\circ$), this difference in values is negligible.

773 In order to estimate the limits of the volume of water trapped within RecAR, we
 774 followed Flierl (1981) defining the volume of trapped water in an eddy as the envelope
 775 of depths enclosed within the outer eddy limit where the azimuthal speed is equal to or
 776 higher than the translating speed of the eddy. For that, we computed the translation speed
 777 of the eddy during the period of time of interest using the trajectory of the geometri-
 778 cal center of the eddy computed by TOEddies. The resulting median translation speed
 779 is 5.7 with a STD of $1.4 \times 10^{-2} \text{ m s}^{-1}$.

780 We then identified the line delimiting the trapped water inside RecAR (called sep-
 781 aratrix here, following De Steur et al. (2004)) by hypothesizing that the eddy is circular
 782 and is moving at a constant speed. The black solid line in Figure 13a indicates the

783 approximate location of the separatrix at each depth and the two black dashed lines de-
 784 limit the STD ($1.4 \times 10^{-2} \text{ m s}^{-1}$) of the mean translation speed. The separatrix is located
 785 below a depth of 1000 m and at less than ~ 100 km from the eddy center. It should be
 786 noted here that 1000 m is the parking depth for most of the core Argo floats. The fact
 787 that the eddy is coherent at this depth explains why the Argo float No. 5902281 remained
 788 trapped within the structure for so long.

789 We also compared the steady horizontal velocity structure of RecAR with the eddy
 790 evolving surface geostrophic velocities derived from satellite altimetry. Figure 13b shows
 791 the various surface geostrophic velocity profile derived from satellite altimetry and pro-
 792 vided by AVISO (in colors, starting in November 2012 with the blue color and ending
 793 in Oct. 2013 with the red color) as well as the velocity profile at a depth of 200 m (black
 794 solid line). The latter corresponds to the white dashed line in Figure 13a and depicts the
 795 position at which the azimuthal velocities reach a maximum. During the period of time
 796 in question, the V_{\max} derived from satellite altimetry decreased with time from 35×10^{-2}
 797 m s^{-1} to $15 \times 10^{-2} \text{ m s}^{-1}$ while $R_{V_{\max}}$ remained approximately constant (Figure 3a).
 798 Therefore, in less than a year, the surface geostrophic velocity corresponding to the eddy
 799 position dropped to half the value of the mean RecAR subsurface geostrophic velocity
 800 intensity. Given the large extent of the Agulhas Ring (both horizontally and vertically)
 801 and its intense thermohaline signature, we suggest that the observed decrease in the sur-
 802 face velocity is not due to a mechanism of dissipation of the eddy, but to the decorre-
 803 lation of the structure main core from the upper water layer attributable to its subduc-
 804 tion during the Fall of 2012. This is confirmed by the hydrological anomalies near the
 805 ocean surface being of opposite sign to those in the eddy subsurface core, as suggested
 806 by Assassi et al. (2016) and Schütte et al. (2016). As a consequence, the surface layer
 807 has an inverse effect on the vertically integrated properties (such as dynamic height, the
 808 eddy geostrophic velocity, etc) compared to that of the eddy at its core. This can ex-
 809 plain, at least partially, the observed decrease in such variables observed since the sub-
 810 duction of the Agulhas Ring.

811 4.4 Integral properties of the subsurface Agulhas Ring

812 We used the separatrix and the 26.2 kg m^{-3} isopycnal surface to identify both the
 813 eddy lower (z_s) and upper (z_0) limits to compute the RecAR volume. This amounts to
 814 $7.1 \times 10^{13} \pm 1.5 \times 10^{13} \text{ m}^3$ where the confidence interval is computed using the STD of

815 the eddy translation speed (as it impacts the volume integration). The temperature and
 816 salinity anomalies integrated between z_s and z_0 for both the Argo profiles and RecAR
 817 are presented in Figure 14. Here, again, a clear relationship appears between these val-
 818 ues and the distance (Dc) from the eddy center. Moreover, the anomalies computed for
 819 RecAR and directly from the Argo profiles are in strong agreement, which supports our
 820 results and methodology.

$$HCA = 2\pi \int_0^{R_s} \int_{z_s}^{z_0} \rho C_p \Delta T r d_r d_z \quad (8)$$

$$SCA = 2\pi \int_0^{R_s} \int_{z_s}^{z_0} \rho \Delta S r d_r d_z \quad (9)$$

821 We estimated the eddy anomalies of heat (HCA) and salt (SCA) from the temper-
 822 ature and salinity anomalies we computed for RecAR and by integrating equations 8 and 9
 823 where $C_p(T)$ is the heat capacity, $\rho(r, z)$ the density, $\Delta T(r, z)$ the conservative temper-
 824 ature anomalies and $\Delta S(r, z)$ the absolute salinity anomalies of RecAR, whereas $R_s(z)$
 825 is the radius of the separatrix. It is then possible to integrate, along the vertical, such
 826 anomalies to assess the total integrated HCA and SCA for RecAR. The values we ob-
 827 tained were, respectively, $2.5 \times 10^{20} \pm 1.3 \times 10^{19}$ J and $6. \times 10^{12} \pm 1.2 \times 10^{11}$ kg where \pm in-
 828 dicates the STD.

829 To be able to compare to simpler estimates not depending on a precise determi-
 830 nation of the eddy volume defined by the separatrix, we integrated the RecAR temper-
 831 ature and salinity anomalies from depths of 1800 to 150 m over the 200 km area around
 832 the eddy center. The values we obtained were 2.9×10^{20} J for HCA and 4.8×10^{12} kg for
 833 SCA. The estimates obtained by the two approaches are very close for HCA whereas they
 834 differ significantly for SCA. This is very likely due to the presence of a negative patch
 835 of AS anomalies not taken into account in the estimates obtained from the first approach
 836 as this patch lies below the eddy trapping depth (Figure 12b).

837 Finally, the instantaneous volume, heat, and salt transport anomalies are computed
 838 following the method introduced by Olson and Evans (1986) and also used by A. M. Dogli-
 839 oli et al. (2007). These physical quantities are obtained by multiplying the integrated
 840 eddy properties with the translation speed divided by the diameter of the structure. They
 841 account for the transport generated by an eddy crossing an imaginary section. For the

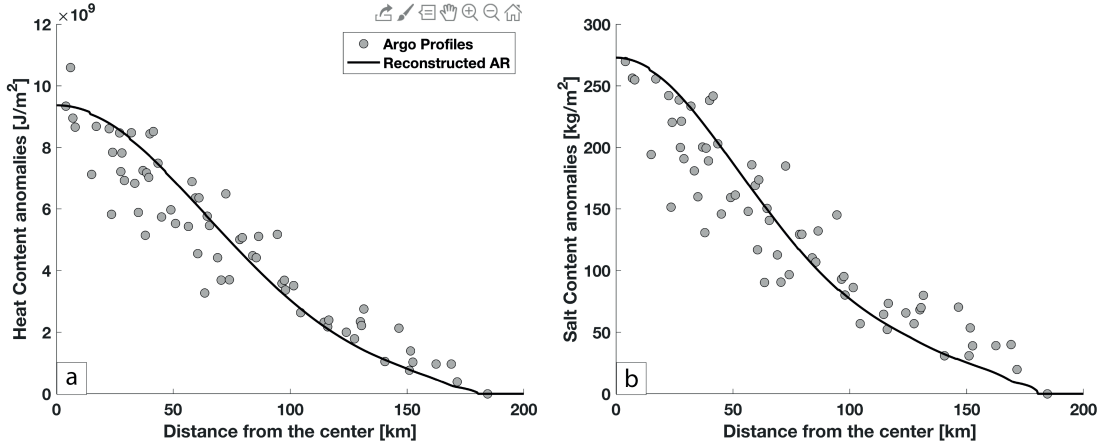


Figure 14. Anomalies of a) Heat Content and b) Salt Content as a function of the distance from the eddy center derived for both the reconstructed Agulhas Ring and the Argo profiles sampling the eddy. These values are obtained by integrating equations 8 and 9 vertically from the eddy separatrix up to 200 m.

842 purposes of calculating transport values, the radius of the volume section was identified
 843 as that of the separatrix that reached the 26.2 kg m^{-3} isopycnal surface. This criteria
 844 led to a radius of 180km. The resulting volume, heat, and salt transports STD are, re-
 845 spectively, $6 \pm 0.5 \text{ Sv}$, $0.02 \pm 0.004 \text{ PW}$, and $5.5 \times 10^5 \pm 1.4 \times 10^5 \text{ kg}^{-1}$. These values are
 846 large as they correspond to the instantaneous transport of an Agulhas Ring. However,
 847 they cannot be used to compare directly with most estimates given in the literature as
 848 these assess the generic impact of Agulhas Rings by dividing the volume, heat, and salt
 849 contents of each eddy by the number of seconds in one year (e.g., van Ballegooyen et al.,
 850 1994; Garzoli et al., 1999). By using this generic approach, the transport of volume, heat,
 851 and salt would amount to, respectively, 2.2 Sv , $8.0 \times 10^{-3} \text{ PW}$, and $2.2 \times 10^5 \text{ kg s}^{-1}$.

852 5 Comparison with Agulhas Rings identified in the literature

853 For more than two decades, numerous Agulhas Rings have been sampled by *in situ*
 854 data. In this section, we compare the subsurface properties of RecAR with 27 different
 855 of those Agulhas Rings described in the literature (see Table 1 for a list of these stud-
 856 ies). This database constitutes an important frame of reference from which to test the
 857 robustness of the properties and characteristics we derived for RecAR (as, for example,
 858 the presence of MWs at its core, or its subsurface nature since crossing the Walvis Ridge).

Table 1. List of all studies having described at least one Agulhas Ring in depth during dedicated oceanographic cruises. It should be noted here that the list is limited to those Agulhas Rings sufficiently documented in the referenced studies.

Article	Number of Eddy
Gordon et al. (1987)	2
M. S. McCartney and Woodgate-Jones (1991)	1
Duncombe Rae et al. (1992)	1
van Ballegooyen et al. (1994)	4
Duncombe Rae et al. (1996)	6
Arhan et al. (1999)	3
Garzoli et al. (1999)	3
McDonagh et al. (1999)	2
Schmid et al. (2003)	1
Gladyshev et al. (2008)	1
Arhan et al. (2011)	1
Casanova-Masjoan et al. (2017)	1
Guerra et al. (2018)	1
TOTAL	27

859 In the following section, we first introduce the general structure of the observed Agul-
860 has Rings before focusing on MWs' properties, with an emphasis on those found within
861 the rings. Finally, we compare estimates of their volume as well as heat and salt con-
862 tents.

863 **5.1 Agulhas Rings general vertical structure and classification**

864 The Agulhas Ring described in this study is characterized by two cores of MW that
865 concentrate the essential fraction of the eddy anomalies when compared to surrounding

866 waters. In this section, we wish to verify whether this is a common albeit not general
867 vertical water mass organization for Agulhas Rings. Out of the 27 referenced eddies, 23
868 were sufficiently described in the literature to be used for the comparison (Gordon et al.,
869 1987; M. S. McCartney & Woodgate-Jones, 1991; Duncombe Rae et al., 1992; van Bal-
870 legooyen et al., 1994; Duncombe Rae et al., 1996; Arhan et al., 1999; Garzoli et al., 1999;
871 McDonagh et al., 1999; Schmid et al., 2003; Gladyshev et al., 2008; Arhan et al., 2011;
872 Casanova-Masjoan et al., 2017; Guerra et al., 2018). We identified as single- or double-
873 core MW eddies those Agulhas Rings whose vertical structure displayed one or two ho-
874 mogeneous layers thicker than 100 m and separated by at least two isotherms of $\theta < 1^\circ\text{C}$
875 and two isohalines of $PSU < .2^\circ$. Each of these eddies were observed during synoptic cruises.
876 Thus they can be associated with a single center position whereas the Agulhas Ring we
877 analyze in this study has been sampled by various Argo profiles along a segment of its
878 trajectory. Hence, it cannot be associated with a single position for its center. Conse-
879 quently, hereinafter we use the averaged location of the segment of trajectory that we
880 reconstructed as the position of RecAR.

881 Of the 24 Agulhas Rings analyzed (i.e. 23 from the literature and our own RecAR),
882 all show at least one core of water with homogeneous hydrological properties, and four
883 exhibit two such cores (see Figure 15a). Three of them were observed northwest of the
884 Cape Basin, as was the case for RecAR, whereas the other was found inside this basin.

885 We also tried to distinguish, among the documented rings in the literature, those
886 eddies that could be considered surface intensified and those (if any) that could be de-
887 scribed as subsurface structures. The classification of eddies as surface or subsurface in-
888 tensified structures is difficult from sparse CTD data. Indeed, due to air-sea interactions,
889 a seasonal thermocline can appear near the ocean surface that might not, necessarily,
890 isolate the eddy structure from the mixing layer during the entire annual cycle. Conse-
891 quently, we have characterized eddies as subsurface intensified according to their shape.
892 Following the schematic view presented by Assassi et al. (2016), subsurface intensified
893 Agulhas Rings are defined as those anticyclones showing a lenticular shape with isopy-
894 cnals on the top of the homogeneous core that are shallower at the eddy center and deeper
895 at the eddy edge. Among such categorization of subsurface eddies, an exception is the
896 eddy described in Guerra et al. (2018) whose structure was derived from a single pro-
897 file. The first homogeneous core documented by Guerra et al. (2018) lies below 100 m.

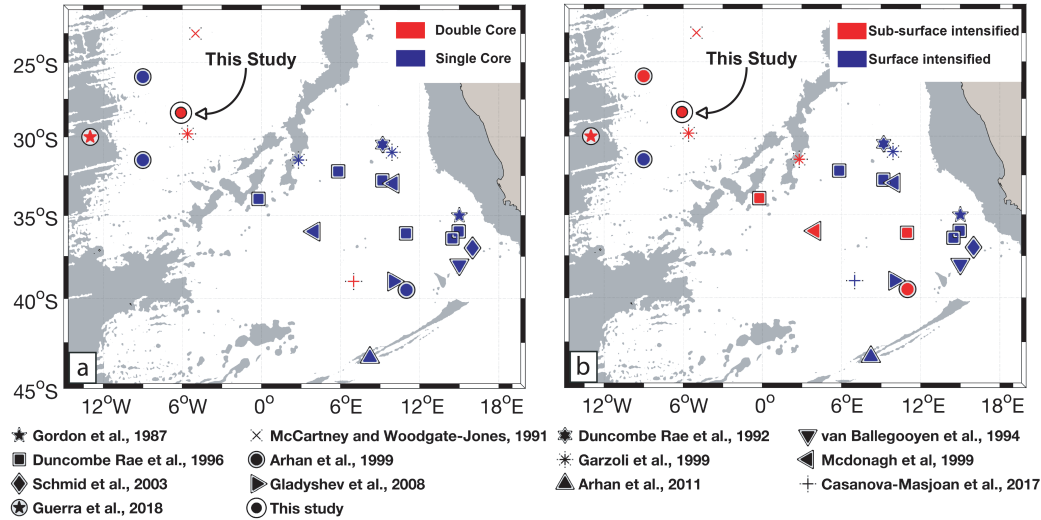


Figure 15. Number of a) cores and b) type of internal structure of the Agulhas Rings described in the literature. Each article is associated with a unique marker type. The gray shading patches in a) represent water depth shallower than 3500 m in the ETOPO2 dataset (Smith & Sandwell, 1997).

898 We associated it with a subsurface eddy, even if the horizontal structure of the eddy was
 899 not provided.

900 Of the 23 Agulhas Rings we selected from the literature, 10 of them (i.e. $\sim 40\%$ are
 901 subsurface intensified and are indicated with red markers in Figure 15b). In general, they
 902 align along the southeast-northwest diagonal in the center of the Cape Basin following
 903 the main Agulhas Rings route (Dencausse et al., 2010; Guerra et al., 2018; Laxenaire et
 904 al., 2018, e.g.) whereas the surface intensified ones (in blue in Figure 15b) lie closer to
 905 the Agulhas Retroflection area and the continental slope of the Cape Basin. It is worth
 906 noting that the eddy observed by Arhan et al. (2011) while it was sitting above the Ag-
 907 ulhas Ridge is also a surface intensified eddy associated with a surface mixed layer depth
 908 of ~ 30 m which capped a homogeneous layer of more than ~ 500 m of thickness (Arhan
 909 et al., 2011). Consequently, Arhan et al. (2011)'s characterization of this eddy as sur-
 910 face or subsurface is not straightforward. Similarly, the eddy described by Casanova-Masjoan
 911 et al. (2017) shows a lenticular shape in salinity but not in temperature nor in poten-
 912 tial density (see Figure 3 in Casanova-Masjoan et al. (2017)). Consequently, its classi-
 913 fication as either a surface or subsurface eddy was also difficult. As its upper part lies

914 very close to the ocean surface we categorized it as a surface intensified eddy. Three of
 915 the subsurface intensified eddies showed a double core with homogeneous properties and
 916 with a very similar vertical structure to RecAR. Like RecAR, two of them were found
 917 in the Southeast Atlantic.

918 In conclusion, we categorized the whole set of Agulhas Rings in four different cat-
 919 egories according to the number of cores with homogeneous properties and whether they
 920 were surface intensified eddies or not.

921 5.2 Agulhas Rings Mode Waters

922 The two-dimensional axisymmetric structure of RecAR has two distinct cores with
 923 homogeneous water properties that fall into the MWs category. As these waters are re-
 924 sponsible for the majority of the eddy heat and salt anomalies (with reference to the en-
 925 vironmental waters), it is important to compare the RecAR properties with similar struc-
 926 tures documented in the literature in order to estimate the commonalities of their prop-
 927 erties as well as their origins. Of the 27 Agulhas Rings identified in previous studies (see
 928 Table 1) that show one or two cores of MW, 5 (i.e. $\sim 20\%$) have their upper limit shal-
 929 lower than 50 m. For these five eddies, the subsurface homogeneous layer has been de-
 930 scribed by the authors of the relevant studies as a deep mixed layer. Deep homogeneous
 931 layers are indeed thought to be the first and necessary phase of MW formation (e.g., Al-
 932 fultis & Cornillon, 2001; Joyce, 2012; Sato & Polito, 2014). These deep mixed layers have
 933 been shown to be common in eddies, and they appear to occur more in anticyclones than
 934 in cyclones (Kouketsu et al., 2012; Sato & Polito, 2014).

935 The hydrological properties of the documented Agulhas Ring MW cores are pre-
 936 sented in Tables G1 and G2 in the Appendix. The position at which these eddies were
 937 sampled and their θ - S characteristics are shown, respectively, in panels a and b of Fig-
 938 ure 16. Figure 16b shows that their properties range from 25.4 to 26.8 kg m^{-3} in σ_0 , from
 939 12 to 19°C in potential temperature, and from 35.08 and 35.75 in (practical) salinity units.

940 As discussed in the Introduction, various MWs are described in the literature. We
 941 have summarized their properties in Table F1 in the Appendix. Even if very similar, they
 942 all show small property differences. Recently, de Souza et al. (2018) discussed a possi-
 943 ble contribution of distinct MWs to South Atlantic Central Water (SACW). However,

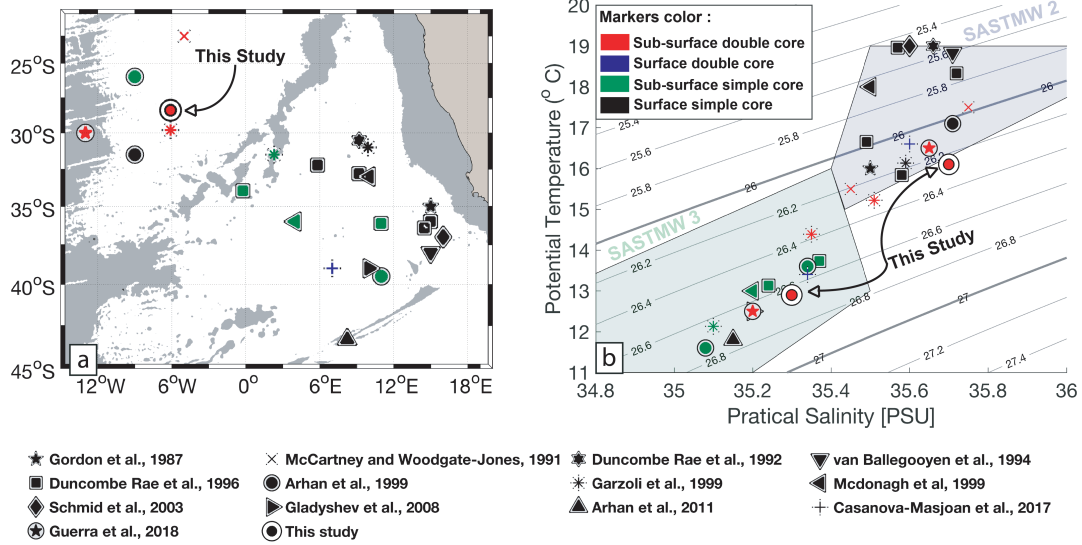


Figure 16. a) Position and b) hydrological properties in the mode water cores of the Agulhas Rings described in the literature. Each study discussing one or more of these eddies is associated with a specific marker and the color corresponds to a particular type of eddy. Double-core mode water eddies have two similar markers. The gray shaded patches in a) represent water depth shallower than 3500 m in the ETOPO2 dataset (Smith & Sandwell, 1997). The background lines in b) represent isopycnals of potential density anomalies referenced to the surface pressure (σ_0). The blue and green shaded patches highlight the hydrological properties of, respectively, SASTMW2 and SASTMW3 as described by Sato and Polito (2014).

944 as they decomposed SACW by MW contribution, the specific hydrological properties of
 945 the various SATMWs cannot be derived directly from that publication.

946 Here, we compared the whole set of Agulhas Ring MWs (that includes RecAR and
 947 all those found in the literature) to Sato and Polito (2014) SATMWs. Figure 16 presents
 948 the Sato and Polito (2014) SATMWs' hydrological distributions as areas shaded in blue
 949 (SASTMW2) and green (SASTMW3). We do not consider here SASTMW1, which is
 950 only found west of 30°W whereas SASTMW2 and SASTMW3 occupy the eastern South
 951 Atlantic sector. SASTMW2 and SASTMW3 are separated by the 35°S parallel (see Fig-
 952 ure 4 in Sato and Polito (2014)).

953 Agulhas Ring MW core properties fall in the range of SASTMW2 and SASTMW3.
 954 Moreover, more than 50% of these Agulhas Ring MW cores have properties within the
 955 generic SASTMW characteristics (see Table F1 in the Appendix). In particular, nearly
 956 all the surface Agulhas Rings that have a single MW core (in black) are in the range of
 957 SASTMW2, whereas the whole set of subsurface Agulhas Rings with a simple MW core
 958 (green) fall in the SASTMW1 category. The only exception is the eddy described by Arhan
 959 et al. (2011), which shows a particularly thick homogeneous layer capped by a narrow
 960 surface layer. We identified it as a surface intensified eddy as the surface layer was only
 961 30 m thick. However, this eddy, observed by the 2008 GoodHope cruise in late Febru-
 962 ary, was clearly at the beginning of a phase described as a subduction by Arhan et al.
 963 (2011) as the eddy disappeared from the altimetry a few months later (at the beginning
 964 of April 2008, (Arhan et al., 2011)). Given the size and energy of this Agulhas Ring, it
 965 is improbable that it simply dissipated so quickly.

966 If we look at the spatial organization of single MW core Agulhas Rings in Figure 16a,
 967 we see that those that are surface intensified mainly lie near the African continental slope
 968 covering the eastern part of the Cape Basin. The subsurface ones, on the other hand,
 969 are essentially found in the central part of the basin, along the Agulhas Ring central path
 970 (Laxenaire et al., 2018).

971 Double-core MW Agulhas Rings have a simpler distribution. Most (4) subsurface
 972 double-core MW rings were observed north/north-west of the Cape Basin. That described
 973 by M. S. McCartney and Woodgate-Jones (1991) shows SASTMW2 characteristics, whereas
 974 the others three (Garzoli et al. (1999), Guerra et al. (2018) and RecAR) have proper-
 975 ties falling in both varieties of SASTMW (see Figure 16b). Only one surface double-core

976 eddy was identified in the literature so far (by Casanova-Masjoan et al. (2017)) lying in
977 the center of the Cape Basin. The MW cores of this show both, SASTMW2 and SASTMW3
978 properties.

979 Arhan et al. (1999) and Arhan et al. (2011) have suggested that Agulhas Ring hy-
980 drological properties are intimately linked to their history. Indeed, these studies have
981 suggested that the route undertaken by these eddies (northern, central or southern ac-
982 cording to Dencausse et al. (2010)), the time they spend within the subantarctic regions,
983 and whether they experience a wintering or not are all factors that determine the wa-
984 ter properties of the upper 1000 m of these structures, mediated by strong air-sea inter-
985 actions and mixing with environmental water. This might explain why, even if some cor-
986 respondence between geographical regions and Agulhas Ring characteristics appear, there
987 seems not to be a clear pattern. On the other hand, Garzoli et al. (1999) and Gladyshev
988 et al. (2008) have suggested that Agulhas Rings displaying a multiple core structure might
989 be explained either by the merging of two rings with distinct histories or by two consec-
990 utive mode water formations during consecutive years.

991 Our study cannot completely explain the origins and diversity of Agulhas Ring MW
992 properties and structure. Indeed, while the formation of the upper MW core was well
993 captured by the profiles achieved by Argo float No. 5902281 during the time it was trapped
994 within the eddy core, we do not have any information on the MW ventilation of the sec-
995 ond and deeper one. The whole set of profiles that sampled Segments 1, 2, and 3 before
996 they merged into Segments 4 and 5 (see Figure 2) did not sample the eddy structures
997 close to the center so they cannot be assumed to characterize the inner eddy vertical struc-
998 ture. It should be noted that Segment 1 spent an entire winter south of 40°S, in the strong
999 westerlies blowing in the subantarctic region, before merging with Segment 4 to form Seg-
1000 ment 5. Segment 1 is very close, albeit it crossed the Walvis Ridge slightly north of the
1001 eddy observed by Arhan et al. (2011). This could explain the fact that both eddies dis-
1002 play SASTMW2 characteristics, but that the deeper core of RecAR is relatively warmer
1003 and saltier than the homogeneous layer of the eddy discussed by Arhan et al. (2011), sug-
1004 gesting that RecAR underwent less intense air-sea interactions. Other published stud-
1005 ies have suggested that MWs observed within Agulhas Rings are or might derive from
1006 modified (Indian) SAMW (e.g., Arhan et al., 1999; Gladyshev et al., 2008) or Subtrop-
1007 ical Indian MW (de Souza et al., 2018). However, the definitions of these two MWs are
1008 not precise (see Table F1 in the Appendix) and this prevents any clear conclusion. We

1009 can merely suggest that Agulhas Rings are large coherent structures advecting, south
 1010 of Africa, Agulhas Current waters (i.e., Subtropical Indian waters). These waters are trans-
 1011 formed along the way by ocean-atmosphere interactions. As suggested by Arhan et al.
 1012 (2011), these exchanges, when occurring during winter, give rise to episodes of intense
 1013 convection that are accompanied by lateral mixing with environmental water. Indeed,
 1014 the large cooling and freshening of the homogeneous layer waters can be explained only
 1015 by taking into account both processes. Moreover, the more intense the convection, the
 1016 larger the mixing and therefore the greater the cooling and freshening. This can eluci-
 1017 date why the eddy observed by Arhan et al. (2011) southward of Segment 1’s actual tra-
 1018 jectory showed lower temperature and salinity than RecAR.

1019 The precise processes involved in the formation of relatively deep mixed layers within
 1020 Agulhas Rings and how these layers transform into MW cores have not been directly ob-
 1021 served. However, by using very high-resolution numerical simulations, Capuano et al.
 1022 (2018) showed that submesoscale instabilities (of different type) are responsible for both
 1023 deep mixing layer formation during winter and the upper-layer restratification during
 1024 summer as discussed in Section 3.2 describing possible mechanisms of subduction. More-
 1025 over, this type of instability leads to mixing layer water subduction and the formation
 1026 of a local variety of mode water that the authors defined as Agulhas Ring Mode Water
 1027 (ARMW) and whose properties depend on the eddy history. These numerical results,
 1028 as well as our analyses on the observed Agulhas Ring MW properties, would suggest that
 1029 MWs found in Agulhas Ring cores are formed within these eddies and not a regional va-
 1030 riety of SASTMW corresponding to a more classical and larger-scale definition of wa-
 1031 ter mass subduction. Yet, from the *in situ* data we have analyzed we are not able to re-
 1032 construct the entire evolution of RecAR, neither are we able to demonstrate unequiv-
 1033 ocaly that ARMWs are the same water masses as SASTMW2 and SASTMW3, nor that
 1034 they can be found only within eddies.

1035 **5.3 Agulhas Rings volume transport, and heat and salt contents**

1036 Table 2 presents the estimates of the volume as well heat and salt content anoma-
 1037 lies for 17 of the 27 Agulhas Rings found in the literature for which at least one of these
 1038 values was provided by the authors of the studies in question. When the authors give
 1039 more than one value for these variables for one eddy, we only provide those estimates
 1040 computed using the closest boundaries of integration to ours.

1041 The average Agulhas Ring volume, HCA, and SCA in the literature are, respec-
 1042 tively, $3.4 \times 10^{13} \pm 1.6 \times 10^{13} \text{ m}^{-3}$, $1.0 \times 10^{20} \pm 0.7 \times 10^{20} \text{ J}$, and $5.2 \times 10^{12} \pm 3.6 \times 10^{12} \text{ kg}$. Hence
 1043 RecAR proves to be one of the strongest and largest Agulhas Rings ever observed. The
 1044 estimated volume and HCA are more than double that of the Agulhas Ring documented
 1045 values, and the SCA is slightly higher than their average.

1046 All rings, with the exception of RecAR and two others (M. S. McCartney & Woodgate-
 1047 Jones, 1991; Garzoli et al., 1999), were found in the Cape Basin. It might therefore be
 1048 possible that the large values of RecAR for both HCA and SCA are due to a lateral mix-
 1049 ing with surrounding waters. However, the fact that the waters trapped within the eddy
 1050 show different properties from the environment and the MW cores are similar to those
 1051 found in other Agulhas Rings gives us confidence that RecAR is a coherent mesoscale
 1052 eddy advecting modified Indian waters into the South Atlantic. Beyond these conjec-
 1053 tures, we can compare assessments of these integrated properties for RecAR and the rings
 1054 documented in the literature by using the same approach as in the related articles. The
 1055 results are presented in Table H1 in the Appendix where the values given in the articles
 1056 are expressed as a percentage of the values for the same variables obtained for RecAR.
 1057 This comparison shows that, even if we do not consider the upper 200 m of the water
 1058 column for RecAR, it still results in the largest volume. RecAR is also one of the rings
 1059 with the highest hydrological anomalies, higher than all but 2 and 4 of the other 16 for,
 1060 respectively, RecAR HCA and SCA. However, these rings were observed close to the Ag-
 1061 ulhas Retroreflection area.

1062 **6 Summary and conclusions**

1063 We have analyzed the evolution of a long-lived Agulhas Ring during 1.5 years of
 1064 its lifespan by simultaneously using a new eddy-tracking algorithm (TOEddies) applied
 1065 to satellite altimetry maps and Argo floats to uncover the eddy's hydrological proper-
 1066 ties. This eddy was sampled by a large number of Argo profiles (71) between the north-
 1067 ern region of the Cape Basin and the Mid-Atlantic Ridge, similarly to the eddies discussed
 1068 by J. M. A. C. Souza et al. (2011) and Nencioli et al. (2018). In particular, one of the
 1069 Argo floats (No. 5902281) remained trapped within the eddy core for 14 months (from
 1070 October 2012 to November 2013), which provided a vertical snapshot of the eddy every
 1071 10 days. We also selected all additional Argo profiles lying at less than 200 km from the
 1072 eddy center. However, we made a careful distinction between the profiles sampling the

Table 2. Integrated properties of Agulhas Rings described in the literature. The reference for the bottom limit of integration is given in the last column. The integrations are achieved either from an isotherm for a fixed depth or by identifying the coherent part of the eddy assessed, following Flierl (1981), as the volume of the eddy where eddy velocities are lower than the eddy drifting speed. The upper limit of integration is the surface for all eddies except RecAR, for which the integration is limited to $\sigma_0=26.2 \text{ kg m}^{-3}$.

Article	Eddy	Volume [m ³]	HCA [J]	SCA[kg]	Reference
McCartney & Woodgate-Jones, (1991)	Eddy	3.6×10^{13}			Trap $5 \times 10^{-2} \text{ m s}^{-1}$
van Ballegooyen et al., (1994)	A3	4.31×10^{13}	1.5×10^{20}	8.74×10^{12}	T > 8° C
van Ballegooyen et al., (1994)	A4	3.94×10^{13}	2.36×10^{20}	13.1×10^{12}	T > 8° C
van Ballegooyen et al., (1994)	A5	1.53×10^{13}	0.73×10^{20}	4.35×10^{12}	T > 8° C
van Ballegooyen et al., (1994)	A6	2.45×10^{13}	1.06×10^{20}	4.59×10^{12}	T > 8° C
Duncombe Rae et al., (1996)	B1-1		0.19×10^{20}	1.21×10^{12}	800 m
Duncombe Rae et al., (1996)	B2-1		0.24×10^{20}	1.52×10^{12}	800 m
Duncombe Rae et al., (1996)	B2-2		0.57×10^{20}	3.8×10^{12}	800 m
Duncombe Rae et al., (1996)	B2-3		0.55×10^{20}	3.72×10^{12}	800 m
Duncombe Rae et al., (1996)	B2-4		0.42×10^{20}	1.67×10^{12}	800 m
Duncombe Rae et al., (1996)	B3-1		0.6×10^{20}	3.88×10^{12}	800 m
McDonagh et al, (1999)	R1	1.5×10^{13}	0.39×10^{20}	2.43×10^{12}	T > 10° C
McDonagh et al, (1999)	R2	4.7×10^{13}	0.44×10^{20}	2.71×10^{12}	T > 10° C
Garzoli et al., (1999)	R-1	2.8×10^{13}	1.33×10^{20}	8×10^{12}	1100 m
Garzoli et al., (1999)	R-2	4.18×10^{13}	1.31×10^{20}		1100 m
Garzoli et al., (1999)	R-3	1.88×10^{13}	0.77×10^{20}		1100 m
Schmid et al., (2003)	JAR	2.8×10^{13}	1.71×10^{20}	10.7×10^{12}	1100 m
This study	RecAR	7.1×10^{13}	2.5×10^{20}	6.8×10^{12}	Trap $6 \times 10^{-2} \text{ m s}^{-1}$

1073 eddy within its boundaries and those characterizing the environment. This was possi-
1074 ble as the TOEddies method automatically computes, for every detected eddy, its outer
1075 and characteristic contours together with the evolution of its surface properties.

1076 The eddy we discussed in this study corresponds to a segment of an Agulhas Ring
1077 main trajectory (according to the definition of Laxenaire et al. (2018)) that has been tracked
1078 by TOEddies for 4 years and 7 months (from January 2011 to July 2015). This segment
1079 was generated in the Cape Basin by the merging of three different Agulhas Rings. Along
1080 this segment the eddy proved to be particularly coherent in its shape whereas its sur-
1081 face ADT anomaly, velocity, and $-Ro-$ decreased with time, as previously observed
1082 for other rings (e.g., Byrne et al., 1995; Schouten et al., 2000; Guerra et al., 2018; Lax-
1083 enaire et al., 2018).

1084 The subsurface observations of the eddy were characterized by two distinct peri-
1085 ods: one in austral winter, during which the mixing layer in the eddy deepened signif-
1086 icantly, and a second in austral summer, during which the upper hydrological core of the
1087 eddy subsided while propagating west. We showed that the eddy, when capped by sur-
1088 face warmer layers, is characterized by negative SST anomalies that support, according
1089 to Assassi et al. (2016), its characterization as a subsurface intensified eddy. This study
1090 represents, to our knowledge, the first Lagrangian evidence of the subduction of an Ag-
1091 ulhas Ring. This result is supported by previous observations of a subducted Agulhas
1092 Ring (Arhan et al., 1999) and numerical studies by Herbette et al. (2004). However, from
1093 the data we have analyzed, we cannot infer precisely the mechanism that acted to sep-
1094 arate the coherent part of the eddy from the upper layers. Indeed, we document the pres-
1095 ence of significantly different water masses in the Agulhas Ring compared with the en-
1096 vironment. The upper-layer hydrological properties of the Agulhas Ring appear differ-
1097 ent from the environment, too, but they are also distinct from those of the eddy core be-
1098 low. This indicates a clear separation of the Agulhas Ring core from the surface, result-
1099 ing in a less coherent upper-layer behavior that enables the Agulhas Ring and surround-
1100 ing waters to mix (e.g., Wang et al., 2015), producing modified water of Indian-Atlantic
1101 origins. Hence, for the particular Agulhas Ring discussed in this study, it appears that
1102 the eddy still influences the velocity in the surface waters rather than being completely
1103 separated.

1104 The transition from a surface to a subsurface intensified eddy concomitant with the
1105 trapping of a profiling float is of a great interest in light of the question about the abil-
1106 ity of eddy detection methods to detect coherent eddies (e.g., Abernathey & Haller, 2018)
1107 from a surface field. In the same way as in previous studies (J. M. A. C. Souza et al.,
1108 2011; Nencioli et al., 2018), the TOEddies eulerian detection algorithm showed it could
1109 successfully identify and track a coherent eddy as it is able to trap a profiling float for
1110 more than one year. However, the observation of the subduction of the eddy enabled us
1111 to go beyond these results as it documented that a reduction in the eddy surface inten-
1112 sity is not associated with the global dissipation of the structure, but with its subsidence
1113 in the ocean interior. Indeed, the subducted eddy conserves its size and properties, and
1114 the maximum geostrophic velocity seems to move, while subducting, from the ocean sur-
1115 face to a depth of 200 m. In this case, the velocities at the surface still satisfy the trap-
1116 ping water conditions of Flierl (1981) and Chelton et al. (2011). However, we might ex-
1117 pect this to not always be the case for the water column encompassing the surface layer
1118 and the full structure of the eddy at depth. This would result in an incoherent eddy-like
1119 behavior in the surface layer while the deeper layers of the eddy continued to behave as
1120 a coherent structure. Moreover, as the surface geostrophic velocity decreases, we can ex-
1121 pect the signal-over-noise ratio to increase in satellite altimetry maps. This ratio is par-
1122 ticularly important for Lagrangian eddy detection techniques (e.g., Beron-Vera et al.,
1123 2013; Abernathey & Haller, 2018) and it is very sensitive to absolute values of the sur-
1124 face velocities. Therefore we advise caution when analyzing eddies' coherence from sur-
1125 face fields only and, in particular, when estimating the Agulhas Leakage achieved by Ag-
1126 ulhas Ring (e.g., Wang et al., 2015, 2016). Indeed, our results suggest that Agulhas Ring
1127 can behave as a coherent structure, but mainly so within the subsurface layers.

1128 Another possible consequence of the subduction process might be the formation
1129 of mode water layer cores. Indeed, the eddy we studied presented two cores of mode wa-
1130 ters. One of these was very likely linked to the last winter convection as described by
1131 Capuano et al. (2018). A second one, located deeper, was probably linked to a merging
1132 of an Agulhas Ring that took, after being spawned by the Agulhas Retroflection, the South-
1133 ern Route defined by Dencausse et al. (2010) and experienced more intense winter con-
1134 ditions.

1135 Given the long-lasting coherence of the structure after subduction, which shielded
1136 the eddy from any further air-sea exchanges, we assumed it was steady and axisymmet-

1137 ric. This allowed us to reconstruct its three-dimensional hydrological vertical structure
1138 by fitting an alpha Gaussian function (e.g., Carton, 2001; Le Vu et al., 2018; Zeitlin, 2018).
1139 We defined the eddy thermohaline anomalies in relation to the surrounding environment.
1140 These anomalies turned out to be very intense and concentrated within the two mode
1141 water layers, and they concentrated the majority of the anomaly signal distinguishing
1142 this eddy from the surrounding South Atlantic waters. Our reconstruction is similar to
1143 the approach of Nencioli et al. (2018) who studied a different eddy. However, it differs
1144 in the choice of the variables of integration and in the definition of the eddy boundaries.
1145 Indeed, we carefully considered only profiles falling strictly within the eddy limits (lat-
1146 eral and vertical) with a view to accurately representing the eddy thermohaline struc-
1147 ture.

1148 A comparison with 27 other Agulhas Rings described in the literature from oceanographic
1149 cruises shows that we can subdivide them into surface and subsurface intensi-
1150 fied rings. The surface intensified rings mainly lie in the Cape Basin, along the South-
1151 ern Africa slope. Those located along the main ring path that occupies the central part
1152 of the Cape Basin (Laxenaire et al., 2018) are predominantly subsurface intensified ed-
1153 dies. Moreover, the rings for which we have found in the literature a vertical section of
1154 their thermohaline properties are all characterized by the presence of at least one core
1155 of mode waters. Some of them show two mode water cores (including the eddy we fo-
1156 cus on in this study). For these, all but one are located in the South Atlantic, north of
1157 the Cape Basin. Hence, the results of the comparison suggest that the subsurface eddy
1158 we reconstructed in this work, which is composed of two homogeneous cores, is not an
1159 exception. Moreover, this analysis provides indications that Agulhas Rings follow a ge-
1160 ographical pattern according to their history and water mass properties. Such a distri-
1161 bution needs to be investigated further from updated data, complementary modeling stud-
1162 ies, and by applying reproducible quantitative methods.

1163 The mode waters found in Agulhas Rings show very variable properties that fall
1164 within the range of two varieties of SASTMW (Sato & Polito, 2014) and in the upper
1165 (warmer and saltier) range of SAMW (M. S. McCartney & Woodgate-Jones, 1991). How-
1166 ever, the continuity of their θ -S properties would rather suggest that these eddies are as-
1167 sociated with one specific variety of mode water formed within Agulhas Rings during the
1168 austral winter (the so-called ARMW as suggested from modeling studies by Capuano
1169 et al. (2018)) and not to different types of mode waters formed remotely. Indeed, south

1170 of Africa the ocean is submitted to intense wind forcing and buoyancy exchanges that
 1171 affect in particular the warm and salty Agulhas Current and Agulhas Rings (e.g., van
 1172 Ballegooyen et al., 1994; Arhan et al., 1999, 2011). The assorted properties observed for
 1173 ARMWs might be due to the different amplitude of such air-sea fluxes as these vary ac-
 1174 cording to the path undertaken by the rings, as well to the synopticity of the atmospheric
 1175 forcing that can vary from one week to another as well as one year from the following,
 1176 or according to the time the rings spend in the area as they can be blocked for several
 1177 months by the interaction with the local topography (e.g., Arhan et al., 1999, 2011). Yet
 1178 our study cannot assess whether the formation of the observed mode waters are restricted
 1179 to Agulhas Rings only, nor can it define the origin of the observed mode waters for the
 1180 double-core rings. The latter might indeed be the result of convection within an eddy
 1181 during two consecutive winters or of the merging of two rings that took different routes
 1182 and underwent different weather conditions (Garzoli et al., 1999). Also, the deeper mode
 1183 water core could be a remnant of SAMW advected within the Agulhas Current from the
 1184 Indian Ocean and already present in the eddy at the moment it was spawned from that
 1185 current.

1186 We calculated the geostrophic velocity of the reconstructed eddy from the nonlin-
 1187 ear thermal wind relation. The maximal value of the azimuthal velocity (0.3 m s^{-1}) was
 1188 found at 200 m and had the same radius as the speed radius derived from satellite al-
 1189 timetry. The surface maximum azimuthal velocity was more intense (up to 0.35 m s^{-1})
 1190 than its subsurface expression from Nov 2012 to January 2013. After this period it de-
 1191 creased steadily to reach 0.15 m s^{-1} at the end of the Argo float No. 5902281 observ-
 1192 ing period. This is a consequence of the eddy subduction that implies at least a partial
 1193 disconnection of the eddy from the ocean surface. Our analysis suggests that the eddy
 1194 extended, after subduction, from a depth of 200-1200 m. We estimated its volume at $7.1 \times 10^{13} \pm$
 1195 $1.5 \times 10^{13} \text{ m}^{-3}$. The heat and salt anomalies transported by the eddy amounted to, re-
 1196 spectively, $4 \text{ }^\circ\text{C}$ and 0.6 g kg^{-1} at a depth of 600 m and the total integrated Heat Con-
 1197 tent Anomalies (HCA) and Salt Content Anomalies (SCA) were estimated at $2.5 \times 10^{20} \pm$
 1198 $0.1 \times 10^{20} \text{ J}$ and $6.8 \times 10^{12} \pm 0.1 \times 10^{12} \text{ kg}$, respectively. Both the volume and the hydro-
 1199 logical anomalies proved to be particularly large when compared with comparable es-
 1200 timates for Agulhas Rings found in the literature. Only Agulhas Rings close to the Ag-
 1201 ulhas Retroreflection show comparably large integrated hydrological anomalies (e.g., van
 1202 Ballegooyen et al., 1994; Arhan et al., 1999, 2011; Schmid et al., 2003).

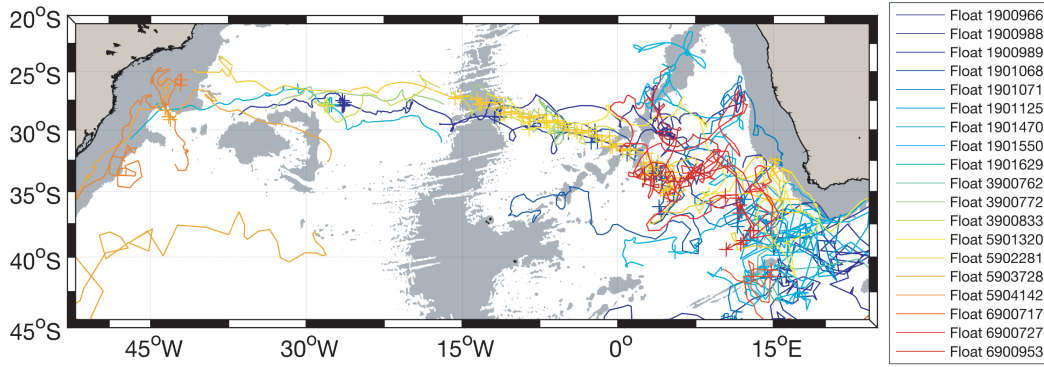


Figure A1. Trajectories and names of the profiling floats that sampled the AREN of interest.

The profiles used in this study are marked by crosses.

1203 Our analysis sheds light on the complex evolution of Agulhas Rings that split and
 1204 merge, undergo intense ventilation, and subduct but remain intense while crossing the
 1205 South Atlantic basin. They advect very large quantities of water, heat, and salt from the
 1206 Indian Ocean. South of Africa, Agulhas Ring waters are (at least partially) modified by
 1207 winter convection that produces thick cores of mode waters. It is in these mode water
 1208 cores that the strongest heat anomaly of these intense eddies seems to reside, when they
 1209 are advected in the South Atlantic Ocean. This, together with the numerous eddy merg-
 1210 ing and splitting occurrences, strongly suggests that the use of exclusively satellite al-
 1211 timetry maps to characterize the coherence of eddies has limitations and that coupling
 1212 with Argo profiles is very useful.

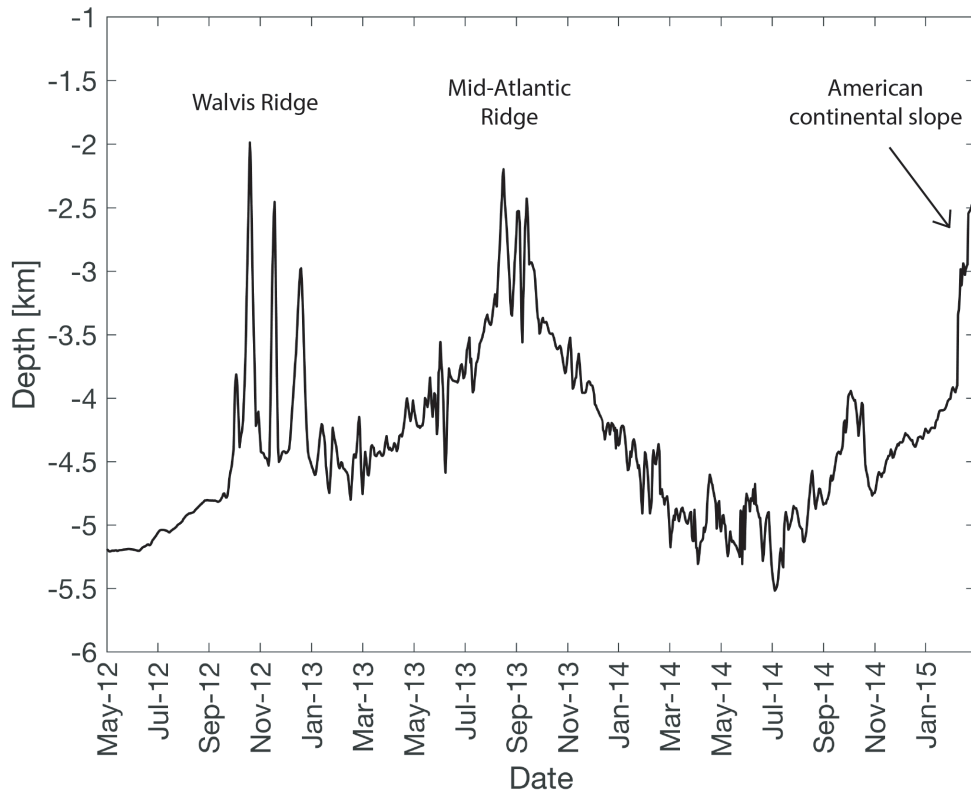


Figure B1. Bathymetry below the fifth trajectory segment of the Agulhas Ring main trajectory studied in this work from the ETOPO2 dataset (Smith & Sandwell, 1997).

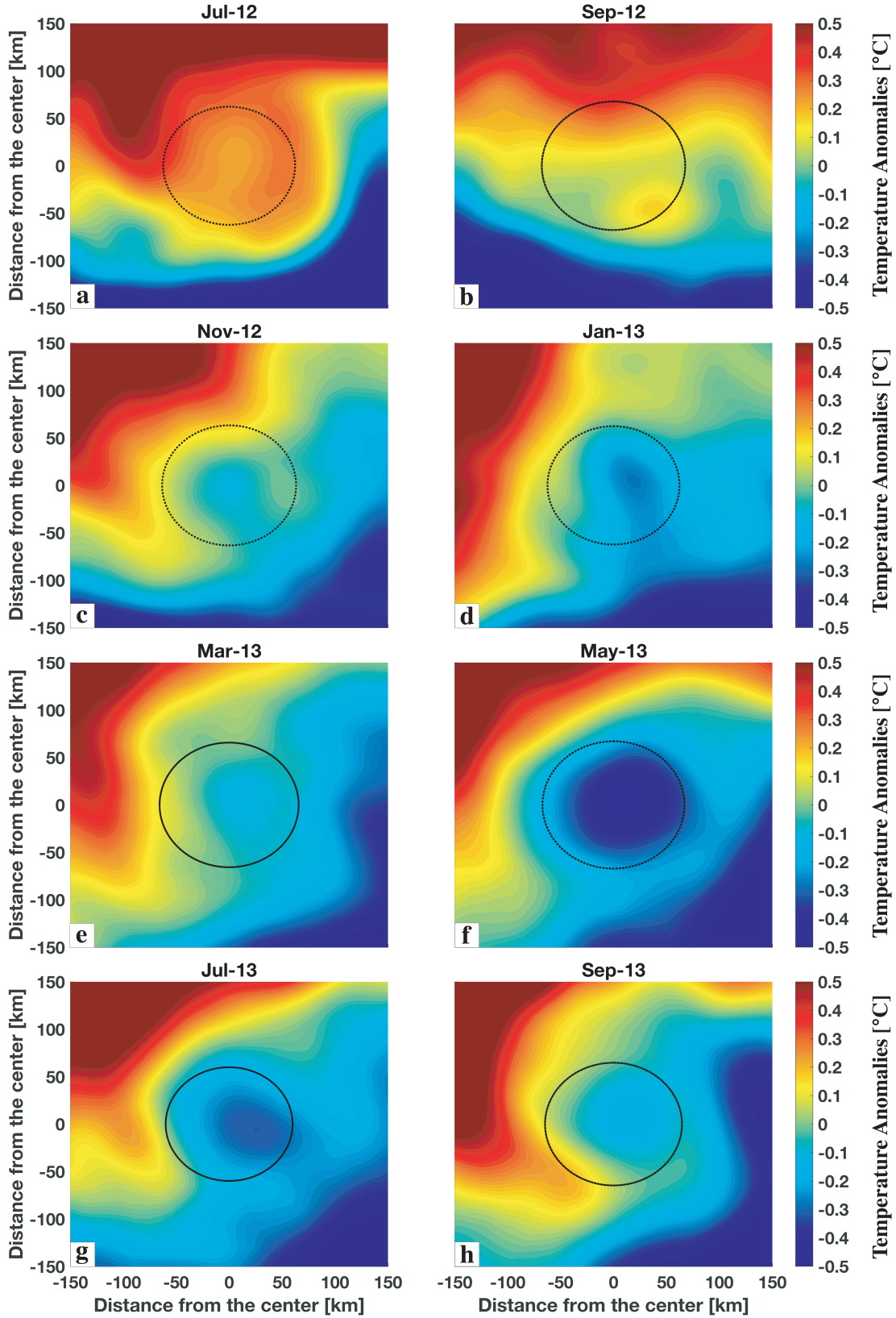


Figure C1. Monthly averaged SST anomalies in the moving reference frame of the 5th segment of the AREN interpolated from the ODYSSEA SST dataset (Dash et al., 2012; Martin et al., 2012). These anomalies are computed by subtracting the mean SST in each panel from the SST values at each point.

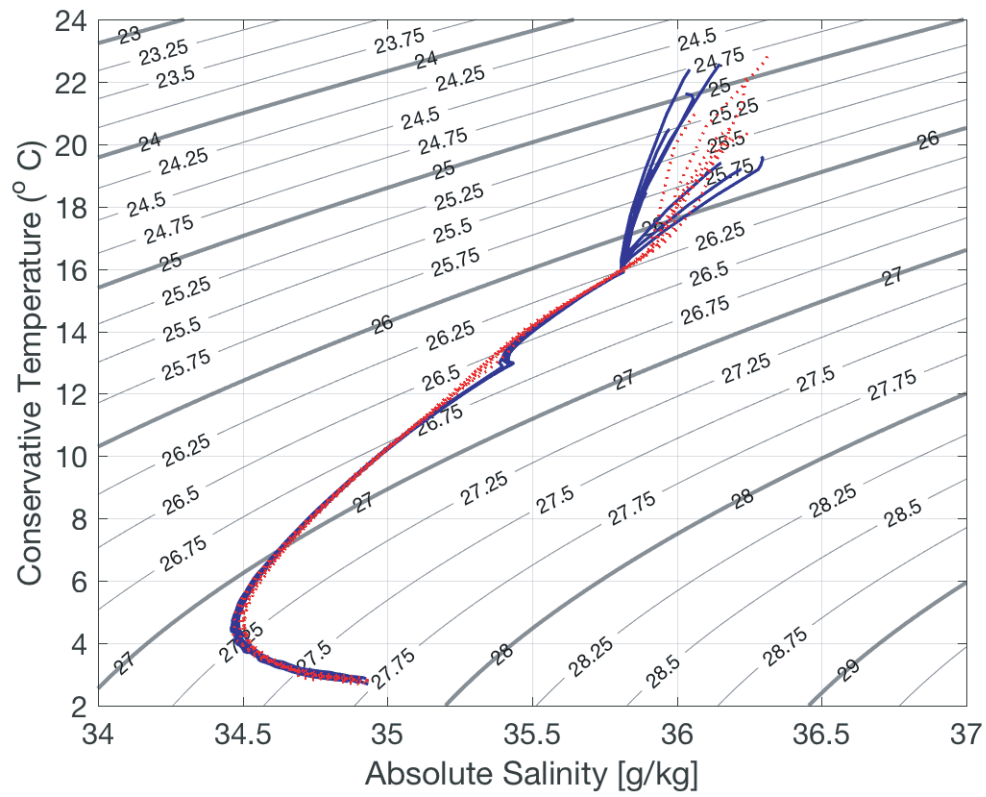


Figure D1. CT-S diagram of Argo profiles with a $D_c < 25$ km in red and those with a $150 < D_c < 200$ km in blue sampling segment 5 between November 2012 and November 2013.

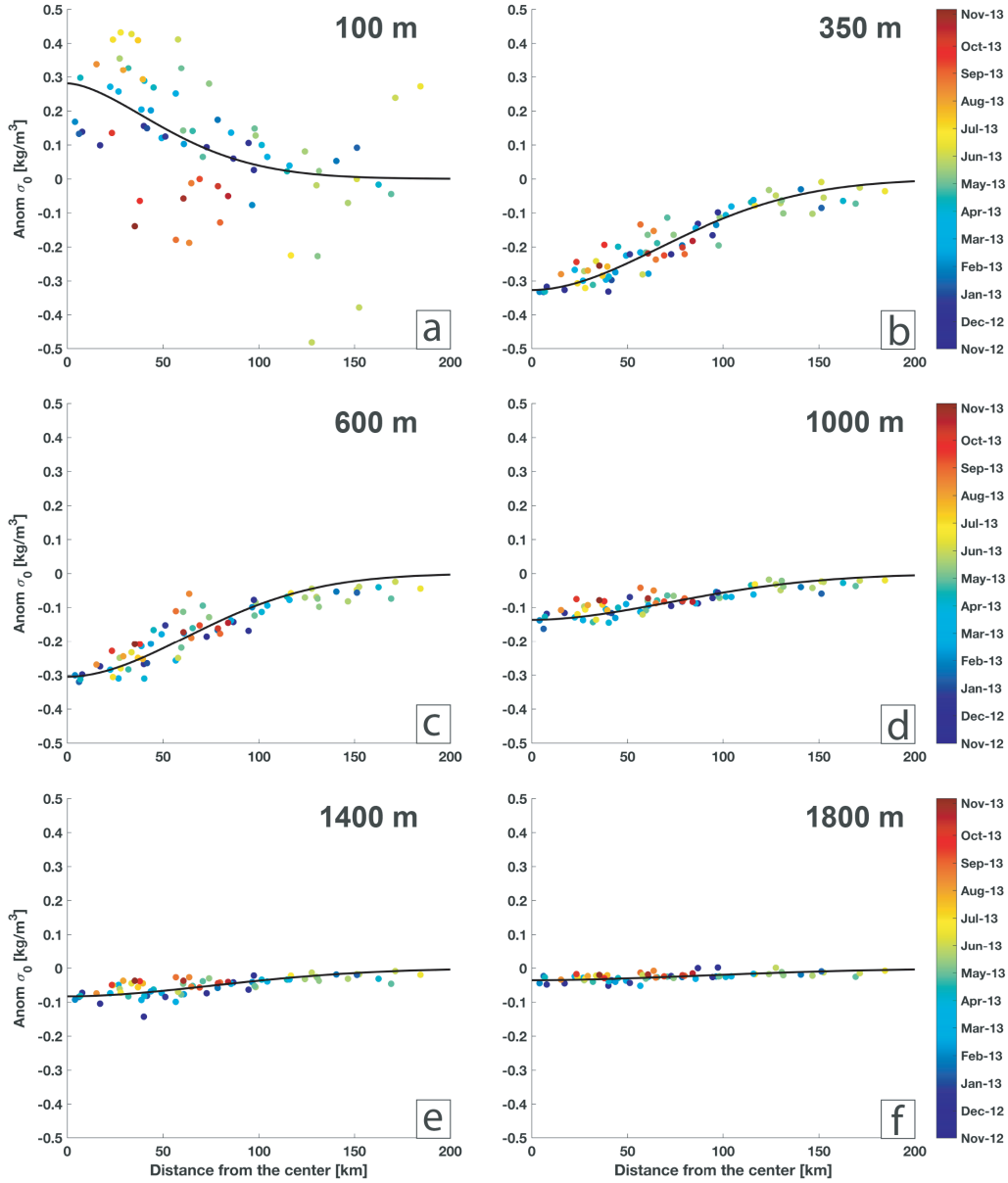


Figure E1. σ_0 anomalies derived from Argo observations (circles) and from the reconstructed Agulhas Ring (solid black lines) at 6 different depths as a function of the distance from the eddy center (D_c). The date for each observation is indicated by the color of the circles.

Table F1. Hydrological properties Potential Temperature (θ in $^{\circ}\text{C}$), Practical Salinity (S in PSU) and Potential Density (σ_{θ} in kg m^{-3}) of mode waters found in the South Atlantic as described in the literature. The standard deviations (STD) is provided using the \pm symbol when it is explicitly supplied in the articles.

Acronym	Full Name	θ [$^{\circ}\text{C}$]	PSU [psu]	σ_{θ} [kg m^{-3}]	Reference
SAMW	Subantarctic MW	4-15	34.2-35.8	26.5-27.1	McCartney [1977,1982]
SASTMW	South Atlantic STMW	12-18	35.2-36.2	26.2-26.6	Provost et al. [1999]
SAESTMW	South Atlantic Eastern STMW	15-16	35.4	26.2-26.3	Provost et al. [1999]
SASTMW1	South Atlantic STMW 1	15.0 ± 0.9	35.6 ± 0.2	26.4 ± 0.1	Sato & Polito [2014]
SASTMW2	South Atlantic STMW 2	16.7 ± 0.9	35.7 ± 0.2	26.1 ± 0.1	Sato & Polito [2014]
SASTMW3	South Atlantic STMW 3	13.2 ± 0.9	35.2 ± 0.2	26.5 ± 0.1	Sato & Polito [2014]
STMW ₁₈	STMW $\theta=18$	18 ± 0.56	35.8 ± 0.11	25.9	de Souza et al. [2018]
STMW ₁₄	STMW $\theta=14$	14 ± 0.53	35.40 ± 0.01	26.5	de Souza et al. [2018]
STMW ₁₂	STMW $\theta=12$	12 ± 0.50	35.03 ± 0.14	26.6	de Souza et al. [2018]
SIMW	Subtropical Indian MW	17 ± 0.28	35.57 ± 0.54	26.0	de Souza et al. [2018]

Table G1. Properties of the Agulhas Ring cores described in the literature. The precision of the variables is not fixed as it depends on each article.

Article	Eddy/Core Number	Depth [m]	Thickness [m]	θ [$^{\circ}$ C]	PSU []
Gordon et al., 1987	CTE.1	-230	200	16	35.5
McCartney and Woodgate-Jones, 1991	Eddy.1	-150	100	17.5	35.75
McCartney and Woodgate-Jones, 1991	Eddy.2	-250	100	15.5	35.45
Duncombe Rae et al., 1992	Ring.1	-50	100	19	35.66
van Ballegooyen et al., 1994	A4.1	-70	140	18.83	35.71
Duncombe Rae et al., 1996	B1-1.1	-150	300	16.65	35.49
Duncombe Rae et al., 1996	B2-1.1	-300	400	13.13	35.24
Duncombe Rae et al., 1996	B2-2.1	-100	200	15.84	35.58
Duncombe Rae et al., 1996	B2-3.1	-50	100	18.33	35.72
Duncombe Rae et al., 1996	B2-4.1	-100	200	18.96	35.57
Duncombe Rae et al., 1996	B3-1.1	-300	400	13.73	35.37
Arhan et al., 1999	R1.1	-325	350	11.6	35.08
Arhan et al., 1999	R2.1	-150	120	17.1	35.71
Arhan et al., 1999	R3.1	-350	300	13.6	35.34
McDonagh et al, 1999	R1.1	-325	450	13	35.2
McDonagh et al, 1999	R2.1	-150	100	18	35.5

Table G2. Properties of the Agulhas Ring cores described in the literature. The precision of the variables is not fixed as it depends on each article.

Article	Eddy.Core Number	Depth [m]	Thickness [m]	Pt0 [° C]	PSU []
Garzoli et al., 1999	R-1.1	-100	200	16.13	35.59
Garzoli et al., 1999	R-2.1	-510	140	12.13	35.1
Garzoli et al., 1999	R-3.1	-270	100	15.22	35.51
Garzoli et al., 1999	R-3.2	-350	150	14.39	35.35
Schmid et al., 2003	JAR.1	-50	100	19	35.6
Gladyshev et al., 2008	E3.1	-400	500	12.5	35.2
Arhan et al., 2011	Eddy M.1	-380	550	11.8	35.15
Casanova-Masjoan et al., 2017	ACR.1	-145	170	16.6	35.6
Casanova-Masjoan et al., 2017	ACR.2	-400	100	13.4	35.34
Guerra et al., 2018	Lilian.1	-200	160	16.5	35.65
Guerra et al., 2018	Lilian.2	-480	240	12.5	35.2
This study	AR.1	-290	180	16.1	35.7
This study	AR.2	-560	100	12.9	35.3

Table H1. Integrated properties of the Agulhas Rings described in the literature expressed as percentage of the same variables obtained for RecAR using the same parameter to compute the maximum depth of integration. We do not compare volume for a fixed depth as this is not relevant here.

Article	Eddy	Volume	HCA	SCA	Reference
McCartney & Woodgate-Jones, (1991)	Eddy	46%			Trap $5 \times 10^{-2} \text{ m s}^{-1}$
van Ballegooyen et al., (1994)	A3	72%	71%	123%	$T > 8^\circ \text{ C}$
van Ballegooyen et al., (1994)	A4	66%	112%	186%	$T > 8^\circ \text{ C}$
van Ballegooyen et al., (1994)	A5	26%	35%	61%	$T > 8^\circ \text{ C}$
van Ballegooyen et al., (1994)	A6	41%	50%	65%	$T > 8^\circ \text{ C}$
Duncombe Rae et al., (1996)	B1-1		8%	16%	800 m
Duncombe Rae et al., (1996)	B2-1		10%	21%	800 m
Duncombe Rae et al., (1996)	B2-2		24%	51%	800 m
Duncombe Rae et al., (1996)	B2-3		23%	50%	800 m
Duncombe Rae et al., (1996)	B2-4		18%	22%	800 m
Duncombe Rae et al., (1996)	B3-1		25%	52%	800 m
McDonagh et al, (1999)	R1	31%	23%	38%	$T > 10^\circ \text{ C}$
McDonagh et al, (1999)	R2	96%	26%	42%	$T > 10^\circ \text{ C}$
Garzoli et al., (1999)	R-1		78%	125%	1100 m
Garzoli et al., (1999)	R-2		77%		1100 m
Garzoli et al., (1999)	R-3		45%		1100 m
Schmid et al., (2003)	JAR		101%	167%	1100 m

1213	Appendix A	Argo profiling float trajectories
1214	Appendix B	Bathymetry below the fifth trajectory segment
1215	Appendix C	SST anomalies
1216	Appendix D	CT-S diagram
1217	Appendix E	Examples of potential anomalies reconstruction
1218	Appendix F	Hydrological properties of Mode Waters found in the South
1219		Atlantic as described in the literature.
1220	Appendix G	Hydrological properties of the Agulhas Ring’s cores de-
1221		scribed in the literature.
1222	Appendix H	Integrated properties of the Agulhas Rings described in
1223		the literature.

1224 **Acknowledgments**

1225 The database produced for this paper and scripts to reproduce the main figures presented
1226 in the results are available at the following: [https://vesg.ipsl.upmc.fr/thredds/catalog/](https://vesg.ipsl.upmc.fr/thredds/catalog/IPSLFS/datapapers/Laxenaire_Database_AR.Recont/catalog.html)
1227 [IPSLFS/datapapers/Laxenaire_Database_AR.Recont/catalog.html](https://vesg.ipsl.upmc.fr/thredds/catalog/IPSLFS/datapapers/Laxenaire_Database_AR.Recont/catalog.html). The gridded satel-
1228 lite altimetry data we used in this work were produced by SSALTO/DUACS and dis-
1229 tributed by the Copernicus Marine Environment Monitoring Service. The Argo data were
1230 collected and made freely available by the International Argo Program and the national
1231 programs that contribute to it (<http://coriolis.eu.org> and [http://www.argo.ucsd](http://www.argo.ucsd.edu)
1232 [.edu](http://www.argo.ucsd.edu)). The Argo Program is part of the Global Ocean Observing System. The GHRSSST
1233 Level 4 ODYSSEA Global Foundation Sea Surface Temperature Analysis product was
1234 created by IFREMER/CERSAT with the support of the European Commission GMES
1235 Framework. This work was supported by the European Union’s Horizon 2020 research
1236 and innovation program under grant agreement no. 633211 (AtlantOS), a CNES-TOSCA
1237 research grant, and the 11-ANR-56-004 SAMOC research grant for SS and RL and the
1238 ANR-Astrid Project DYNED-Atlas (ANR-15-ASMA-0003-01) for AS and RL. The au-
1239 thors received several helpful suggestions for improving an earlier version of this manuscript
1240 from A. Doglioli, I. Borrione and two anonymous reviewers, and their help is gratefully
1241 noted. We also acknowledge the mesoscale calculation server CICLAD (<http://ciclad>
1242 [-web.ipsl.jussieu.fr](http://ciclad-web.ipsl.jussieu.fr)) dedicated to Institut Pierre Simon Laplace modeling effort for
1243 technical and computational support.

References

- 1244
- 1245 Abernathey, R., & Haller, G. (2018). Transport by Lagrangian Vortices in the East-
1246 ern Pacific. *Journal of Physical Oceanography*, *48*(3), 667–685.
- 1247 Alfultis, M. A., & Cornillon, P. (2001). Annual and interannual changes in the
1248 North Atlantic STMW layer properties. *Journal of Physical Oceanography*,
1249 *31*(8), 2066–2086.
- 1250 Amores, A., Melnichenko, O., & Maximenko, N. (2017). Coherent mesoscale eddies
1251 in the North Atlantic subtropical gyre: 3-D structure and transport with ap-
1252 plication to the salinity maximum. *Journal of Geophysical Research: Oceans*,
1253 *122*(1), 23–41.
- 1254 Arhan, M., Mercier, H., & Lutjeharms, J. R. E. (1999). The disparate evolution
1255 of three Agulhas rings in the South Atlantic Ocean. *Journal of Geophysical Re-
1256 search: Oceans*, *104*(C9), 20987–21005. Retrieved from [http://dx.doi.org/
1257 10.1029/1998JC900047](http://dx.doi.org/10.1029/1998JC900047) doi: 10.1029/1998JC900047
- 1258 Arhan, M., Speich, S., Messenger, C., Dencausse, G., Fine, R., & Boye, M. (2011,
1259 Nov). Anticyclonic and cyclonic eddies of subtropical origin in the subantarctic
1260 zone south of Africa. *Journal of Geophysical Research*, *116*(C11). Re-
1261 trieved from <http://dx.doi.org/10.1029/2011JC007140> doi: 10.1029/
1262 2011jc007140
- 1263 Assassi, C., Morel, Y., Vandermeirsch, F., Chaigneau, A., Pegliasco, C., Morrow, R.,
1264 ... others (2016). An Index to Distinguish Surface-and Subsurface-Intensified
1265 Vortices from Surface Observations. *Journal of Physical Oceanography*, *46*(8),
1266 2529–2552.
- 1267 Beron-Vera, F. J., Wang, Y., Olascoaga, M. J., Goni, G. J., & Haller, G. (2013). Ob-
1268 jective detection of oceanic eddies and the Agulhas leakage. *Journal of Physi-
1269 cal Oceanography*, *43*(7), 1426–1438.
- 1270 Biastoch, A., & Böning, C. W. (2013). Anthropogenic impact on Agulhas leakage.
1271 *Geophysical Research Letters*, *40*(6), 1138–1143.
- 1272 Biastoch, A., Böning, C. W., & Lutjeharms, J. R. E. (2008). Agulhas leakage dy-
1273 namics affects decadal variability in Atlantic overturning circulation. *Nature*,
1274 *456*, 489–492. Retrieved from <http://oceanrep.geomar.de/8189/> doi: doi:
1275 10.1038/nature07426
- 1276 Biastoch, A., Böning, C. W., Schwarzkopf, F. U., & Lutjeharms, J. (2009). Increase

- 1277 in Agulhas leakage due to poleward shift of Southern Hemisphere westerlies.
 1278 *Nature*, 462(7272), 495.
- 1279 Branch, M. A., Coleman, T. F., & Li, Y. (1999). A subspace, interior, and conjugate
 1280 gradient method for large-scale bound-constrained minimization problems.
 1281 *SIAM Journal on Scientific Computing*, 21(1), 1–23.
- 1282 Byrne, D. A., Gordon, A. L., & Haxby, W. F. (1995). Agulhas Eddies: A Synoptic
 1283 View Using Geosat ERM Data. *Journal of Physical Oceanography*, 25(5), 902–
 1284 917. Retrieved from [https://doi.org/10.1175/1520-0485\(1995\)025<0902:
 1285 AEASVU>2.0.CO;2](https://doi.org/10.1175/1520-0485(1995)025<0902:AEASVU>2.0.CO;2) doi: 10.1175/1520-0485(1995)025(0902:AEASVU)2.0.CO;
 1286 2
- 1287 Cabanes, C., Thierry, V., & Lagadec, C. (2016, 8). Improvement of bias detection
 1288 in Argo float conductivity sensors and its application in the North Atlantic.
 1289 *Deep Sea Research Part I: Oceanographic Research Papers*, 114, 128–136. doi:
 1290 <http://dx.doi.org/10.1016/j.dsr.2016.05.007>
- 1291 Capuano, T. A., Speich, S., Carton, X., & Blanke, B. (2018). Mesoscale and sub-
 1292 mesoscale processes in the Southeast Atlantic and their impact on the regional
 1293 thermohaline structure. *Journal of Geophysical Research: Oceans*, 123(3),
 1294 1937–1961.
- 1295 Carton, X. (2001). Hydrodynamical Modeling Of Oceanic Vortices [Journal Article].
 1296 *Surveys in Geophysics*, 22(3), 179-263. Retrieved from [http://dx.doi.org/10
 1297 .1023/A%3A1013779219578](http://dx.doi.org/10.1023/A%3A1013779219578) doi: 10.1023/A:1013779219578
- 1298 Casanova-Masjoan, M., Pelegrí, J., Sangrà, P., Martínez, A., Grisolia-Santos, D.,
 1299 Pérez-Hernández, M. D., & Hernández-Guerra, A. (2017). Characteristics
 1300 and evolution of an Agulhas ring. *Journal of Geophysical Research: Oceans*,
 1301 122(9), 7049–7065.
- 1302 Chaigneau, A., Eldin, G., & Dewitte, B. (2009). Eddy activity in the four major
 1303 upwelling systems from satellite altimetry (1992–2007). *Progress in Oceanogra-
 1304 phy*, 83(1), 117–123.
- 1305 Chaigneau, A., Gizolme, A., & Grados, C. (2008). Mesoscale eddies off Peru in
 1306 altimeter records: Identification algorithms and eddy spatio-temporal patterns
 1307 [Journal Article]. *Progress in Oceanography*, 79(2), 106-119.
- 1308 Chaigneau, A., Marie, L. T., Gérard, E., Carmen, G., & Oscar, P. (2011). Ver-
 1309 tical structure of mesoscale eddies in the eastern South Pacific Ocean: A

- 1310 composite analysis from altimetry and Argo profiling floats [Journal Arti-
 1311 cle]. *Journal of Geophysical Research: Oceans*, 116(C11). Retrieved from
 1312 <http://dx.doi.org/10.1029/2011JC007134> doi: 10.1029/2011JC007134
- 1313 Chelton, D. B., Schlax, M. G., & Samelson, R. M. (2011). Global observations
 1314 of nonlinear mesoscale eddies [Journal Article]. *Progress in Oceanogra-*
 1315 *phy*, 91(2), 167-216. Retrieved from [http://www.sciencedirect.com/](http://www.sciencedirect.com/science/article/pii/S0079661111000036)
 1316 [science/article/pii/S0079661111000036](http://www.sciencedirect.com/science/article/pii/S0079661111000036) doi: [http://dx.doi.org/10.1016/](http://dx.doi.org/10.1016/j.pocean.2011.01.002)
 1317 [j.pocean.2011.01.002](http://dx.doi.org/10.1016/j.pocean.2011.01.002)
- 1318 Chelton, D. B., Schlax, M. G., Samelson, R. M., & de Szoeke, R. A. (2007). Global
 1319 observations of large oceanic eddies. *Geophysical Research Letters*, 34(15),
 1320 n/a–n/a. Retrieved from <http://dx.doi.org/10.1029/2007GL030812>
 1321 (L15606) doi: 10.1029/2007GL030812
- 1322 Dash, P., Ignatov, A., Martin, M., Donlon, C., Brasnett, B., Reynolds, R. W., ...
 1323 others (2012). Group for High Resolution Sea Surface Temperature (GHRSSST)
 1324 analysis fields inter-comparisons—Part 2: Near real time web-based level 4
 1325 SST Quality Monitor (L4-SQUAM). *Deep Sea Research Part II: Topical Stud-*
 1326 *ies in Oceanography*, 77, 31–43.
- 1327 Dencausse, G., Arhan, M., & Speich, S. (2010). Routes of Agulhas rings in the
 1328 southeastern Cape Basin [Journal Article]. *Deep Sea Research Part I: Oceanog-*
 1329 *raphic Research Papers*, 57(11), 1406-1421.
- 1330 de Souza, A. G. Q., Kerr, R., & de Azevedo, J. L. L. (2018). On the influence of
 1331 Subtropical Mode Water on the South Atlantic Ocean. *Journal of Marine Sys-*
 1332 *tems*, 185, 13–24.
- 1333 De Steur, L., Van Leeuwen, P., & Drijfhout, S. (2004). Tracer leakage from modeled
 1334 Agulhas rings. *Journal of Physical Oceanography*, 34(6), 1387–1399.
- 1335 Doglioli, A., Veneziani, M., Blanke, B., Speich, S., & Griffa, A. (2006). A La-
 1336 grangian analysis of the Indian-Atlantic interocean exchange in a regional
 1337 model. *Geophysical Research Letters*, 33(14).
- 1338 Doglioli, A. M., Blanke, B., Speich, S., & Lapeyre, G. (2007). Tracking coherent
 1339 structures in a regional ocean model with wavelet analysis: Application to
 1340 Cape Basin eddies. *Journal of Geophysical Research: Oceans*, 112(C5). Re-
 1341 trieved from <http://dx.doi.org/10.1029/2006JC003952> (C05043) doi:
 1342 [10.1029/2006JC003952](http://dx.doi.org/10.1029/2006JC003952)

- 1343 Duacs/AVISO+. (2015). SSALTO/DUACS user handbook:(M) SLA and (M) ADT
1344 near-real time and delayed time products. *CLS-DOS-NT-06-034*, 6, 74.
- 1345 Duacs/AVISO+. (2017). Mesoscale Eddy Trajectory Atlas Product Handbook .
1346 *SALP-MU-P-EA-23126-CLS*, 17.
- 1347 Duncombe Rae, C., Garzoli, S., & Gordon, A. (1996). The eddy field of the south-
1348 east Atlantic Ocean: A statistical census from the Benguela Sources and
1349 Transports Project. *Journal of Geophysical Research: Oceans*, 101(C5),
1350 11949–11964.
- 1351 Duncombe Rae, C., Shillington, F., Agenbag, J., Taunton-Clark, J., & Gründlingh,
1352 M. (1992). An Agulhas ring in the South Atlantic Ocean and its interac-
1353 tion with the Benguela upwelling frontal system. *Deep Sea Research Part A.*
1354 *Oceanographic Research Papers*, 39(11-12), 2009–2027.
- 1355 Faghmous, J. H., Frenger, I., Yao, Y., Warmka, R., Lindell, A., & Kumar, V. (2015).
1356 A daily global mesoscale ocean eddy dataset from satellite altimetry. *Scien-*
1357 *tific Data*, 2, 150028. Retrieved from [http://www.ncbi.nlm.nih.gov/pmc/](http://www.ncbi.nlm.nih.gov/pmc/articles/PMC4460914/)
1358 [articles/PMC4460914/](http://www.ncbi.nlm.nih.gov/pmc/articles/PMC4460914/) doi: 10.1038/sdata.2015.28
- 1359 Flierl, G. R. (1981). Particle motions in large-amplitude wave fields. *Geophysical &*
1360 *Astrophysical Fluid Dynamics*, 18(1-2), 39–74.
- 1361 Froyland, G., Horenkamp, C., Rossi, V., & Van Sebille, E. (2015). Studying an Agul-
1362 has ring’s long-term pathway and decay with finite-time coherent sets. *Chaos:*
1363 *An Interdisciplinary Journal of Nonlinear Science*, 25(8), 083119.
- 1364 Garzoli, S. L., Richardson, P. L., Duncombe Rae, C. M., Fratantoni, D. M., Goñi,
1365 G. J., & Roubicek, A. J. (1999). Three Agulhas rings observed during the
1366 Benguela Current Experiment. *Journal of Geophysical Research: Oceans*,
1367 104(C9), 20971–20985. Retrieved from [http://dx.doi.org/10.1029/](http://dx.doi.org/10.1029/1999JC900060)
1368 [1999JC900060](http://dx.doi.org/10.1029/1999JC900060) doi: 10.1029/1999JC900060
- 1369 Gladyshev, S., Arhan, M., Sokov, A., & Speich, S. (2008). A hydrographic section
1370 from South Africa to the southern limit of the Antarctic Circumpolar Current
1371 at the Greenwich meridian. *Deep Sea Research Part I: Oceanographic Research*
1372 *Papers*, 55(10), 1284–1303.
- 1373 Goni, G., Garzoli, S., Roubicek, A., Olson, D., & Brown, O. (1997). Agulhas ring
1374 dynamics from TOPEX/POSEIDON satellite altimeter data [Article]. *Journal*
1375 *of Marine Research*, 55, 861-883. doi: {10.1357/0022240973224175}

- 1376 Gordon, A. L., & Haxby, W. F. (1990). Agulhas eddies invade the South Atlantic:
1377 Evidence from Geosat altimeter and shipboard conductivity-temperature-depth
1378 survey. *Journal of Geophysical Research: Oceans*, *95*(C3), 3117–3125.
- 1379 Gordon, A. L., Lutjeharms, J. R., & Gründlingh, M. L. (1987). Stratification and
1380 circulation at the Agulhas Retroflection. *Deep Sea Research Part A. Oceanographic Research Papers*, *34*(4), 565–599.
- 1382 Gründlingh, M. L. (1995). Tracking eddies in the southeast Atlantic and southwest
1383 Indian oceans with TOPEX/POSEIDON. *Journal of Geophysical Research: Oceans*, *100*(C12), 24977–24986.
- 1385 Guerra, L. A. A., Paiva, A. M., & Chassignet, E. P. (2018). On the translation of
1386 Agulhas rings to the western South Atlantic Ocean. *Deep Sea Research Part I: Oceanographic Research Papers*, *139*, 104–113.
- 1388 Hanawa, K., & Talley, L. D. (2001). 4 Mode waters. In *International geophysics*
1389 (Vol. 77, pp. 373–386). Elsevier.
- 1390 Herbette, S., Morel, Y., & Arhan, M. (2004). Subduction of a surface vortex under
1391 an outcropping front. *Journal of physical oceanography*, *34*(7), 1610–1627.
- 1392 Ioannou, A., Stegner, A., Le Vu, B., Taupier-Letage, I., & Speich, S. (2017). Dy-
1393 namical Evolution of Intense Ierapetra Eddies on a 22 Year Long Period. *Journal of Geophysical Research: Oceans*, *122*(11), 9276–9298.
- 1395 Joyce, T. M. (2012). New perspectives on eighteen-degree water formation in the
1396 North Atlantic. *Journal of oceanography*, *68*(1), 45–52.
- 1397 Kersalé, M., Lamont, T., Speich, S., Terre, T., Laxenaire, R., Roberts, M. J., ...
1398 Ansonge, I. J. (2018, Sep). Moored observations of mesoscale features in the
1399 Cape Basin: characteristics and local impacts on water mass distributions.
1400 *Ocean Science*, *14*(5), 923–945. Retrieved from [http://dx.doi.org/10.5194/
1401 os-14-923-2018](http://dx.doi.org/10.5194/os-14-923-2018) doi: 10.5194/os-14-923-2018
- 1402 Kouketsu, S., Tomita, H., Oka, E., Hosoda, S., Kobayashi, T., & Sato, K. (2012).
1403 The role of meso-scale eddies in mixed layer deepening and mode water forma-
1404 tion in the western North Pacific. *Journal of oceanography*, *68*(1), 63–77.
- 1405 Laxenaire, R., Speich, S., Blanke, B., Chaigneau, A., Pegliasco, C., & Stegner, A.
1406 (2018, Nov). Anticyclonic Eddies Connecting the Western Boundaries of In-
1407 dian and Atlantic Oceans. *Journal of Geophysical Research: Oceans*, *123*(11),
1408 7651–7677. Retrieved from <http://dx.doi.org/10.1029/2018JC014270> doi:

- 1409 10.1029/2018jc014270
- 1410 Lebedev, K. V., Yoshinari, H., Maximenko, N. A., & Hacker, P. W. (2007). Velocity
1411 data assessed from trajectories of Argo floats at parking level and at the sea
1412 surface [Journal Article]. *IPRC Technical Note*, 4(2), 1-16.
- 1413 Lehahn, Y., d'Ovidio, F., Lévy, M., Amitai, Y., & Heifetz, E. (2011). Long range
1414 transport of a quasi isolated chlorophyll patch by an Agulhas ring. *Geophysical
1415 Research Letters*, 38(16).
- 1416 Le Vu, B., Stegner, A., & Arsouze, T. (2018). Angular Momentum Eddy Detec-
1417 tion and tracking Algorithm (AMEDA) and its application to coastal eddy
1418 formation. *Journal of Atmospheric and Oceanic Technology*, 35(4), 739–762.
- 1419 Lumpkin, R. (2016). Global characteristics of coherent vortices from surface drifter
1420 trajectories. *Journal of Geophysical Research: Oceans*, 121(2), 1306–1321.
- 1421 Martin, M., Dash, P., Ignatov, A., Banzon, V., Beggs, H., Brasnett, B., . . . oth-
1422 ers (2012). Group for High Resolution Sea Surface temperature (GHRSSST)
1423 analysis fields inter-comparisons. Part 1: A GHRSSST multi-product ensemble
1424 (GMPE). *Deep Sea Research Part II: Topical Studies in Oceanography*, 77,
1425 21–30.
- 1426 McCartney, M. (1977). *Subantarctic Mode Water, A Voyage of Discovery, George
1427 Deacon: 70th Anniversary Volume M. Angel*, 103–119. Pergamon, New York.
- 1428 McCartney, M. S. (1982). The subtropical recirculation of mode waters. *J. Mar.
1429 Res*, 40(427.4), 64.
- 1430 McCartney, M. S., & Woodgate-Jones, M. (1991). A deep-reaching anticyclonic eddy
1431 in the subtropical gyre of the eastern South Atlantic. *Deep Sea Research Part
1432 A. Oceanographic Research Papers*, 38, S411–S443.
- 1433 McDonagh, E. L., Heywood, K. J., & Meredith, M. P. (1999). On the structure,
1434 paths, and fluxes associated with Agulhas rings. *Journal of Geophysical Re-
1435 search: Oceans*, 104(C9), 21007–21020.
- 1436 McDougall, T. J., & Barker, P. M. (2011). Getting started with TEOS-10 and the
1437 Gibbs Seawater (GSW) oceanographic toolbox. *SCOR/IAPSO WG*, 127, 1–
1438 28.
- 1439 McWilliams, J. C. (1985). Submesoscale, coherent vortices in the ocean. *Reviews of
1440 Geophysics*, 23(2), 165–182.
- 1441 Mkhinini, N., Coimbra, A. L. S., Stegner, A., Arsouze, T., Taupier-Letage, I., &

- 1442 Béranger, K. (2014). Long-lived mesoscale eddies in the eastern Mediter-
1443 ranean Sea: Analysis of 20 years of AVISO geostrophic velocities. *Jour-*
1444 *nal of Geophysical Research: Oceans*, 119(12), 8603–8626. Retrieved from
1445 <http://dx.doi.org/10.1002/2014JC010176> doi: 10.1002/2014JC010176
- 1446 Morrow, R., & Le Traon, P.-Y. (2012). Recent advances in observing mesoscale
1447 ocean dynamics with satellite altimetry. *Advances in Space Research*, 50(8),
1448 1062–1076.
- 1449 Nencioli, F., Dall’Olmo, G., & Quartly, G. D. (2018). Agulhas ring transport ef-
1450 ficiency from combined satellite altimetry and Argo profiles. *Journal of Geo-*
1451 *physical Research: Oceans*, 123(8), 5874–5888.
- 1452 Nencioli, F., Dong, C., Dickey, T., Washburn, L., & McWilliams, J. C. (2010).
1453 A Vector Geometry–Based Eddy Detection Algorithm and Its Application
1454 to a High-Resolution Numerical Model Product and High-Frequency Radar
1455 Surface Velocities in the Southern California Bight. *Journal of Atmospheric*
1456 *and Oceanic Technology*, 27(3), 564–579. Retrieved from [https://doi.org/](https://doi.org/10.1175/2009JTECH0725.1)
1457 [10.1175/2009JTECH0725.1](https://doi.org/10.1175/2009JTECH0725.1) doi: 10.1175/2009JTECH0725.1
- 1458 Olson, D. B., & Evans, R. H. (1986). Rings of the Agulhas current. *Deep Sea Re-*
1459 *search Part A. Oceanographic Research Papers*, 33(1), 27–42.
- 1460 Owens, W. B., & Wong, A. P. (2009). An improved calibration method for the drift
1461 of the conductivity sensor on autonomous CTD profiling floats by θ -S clima-
1462 tology [Journal Article]. *Deep Sea Research Part I: Oceanographic Research*
1463 *Papers*, 56(3), 450–457.
- 1464 Pegliasco, C., Chaigneau, A., & Morrow, R. (2015). Main eddy vertical structures
1465 observed in the four major Eastern Boundary Upwelling Systems. *Journal of*
1466 *Geophysical Research: Oceans*, 120(9), 6008–6033.
- 1467 Provost, C., Escoffier, C., Maamaatuaiahutapu, K., Kartavtseff, A., & Garçon, V.
1468 (1999). Subtropical mode waters in the South Atlantic Ocean. *Journal of*
1469 *Geophysical Research: Oceans*, 104(C9), 21033–21049.
- 1470 Pujol, M.-I., Faugère, Y., Taburet, G., Dupuy, S., Pelloquin, C., Ablain, M., & Pi-
1471 cot, N. (2016). DUACS DT2014: the new multi-mission altimeter data set
1472 reprocessed over 20 years. *Ocean Science*, 12(5).
- 1473 Rusciano, E., Speich, S., & Ollitrault, M. (2012). Interocean exchanges and the
1474 spreading of Antarctic Intermediate Water south of Africa. *Journal of Geo-*

- 1475 *physical Research: Oceans*, 117(C10).
- 1476 Sato, O., & Polito, P. (2014). Observation of South Atlantic subtropical mode wa-
1477 ters with Argo profiling float data. *Journal of Geophysical Research: Oceans*,
1478 119(5), 2860–2881.
- 1479 Schmid, C., Boebel, O., Zenk, W., Lutjeharms, J., Garzoli, S., Richardson, P., &
1480 Barron, C. (2003). Early evolution of an Agulhas Ring. *Deep Sea Research*
1481 *Part II: Topical Studies in Oceanography*, 50(1), 141–166.
- 1482 Schouten, M. W., de Ruijter, W. P. M., van Leeuwen, P. J., & Lutjeharms, J. R. E.
1483 (2000). Translation, decay and splitting of Agulhas rings in the southeastern
1484 Atlantic Ocean. *Journal of Geophysical Research: Oceans*, 105(C9), 21913–
1485 21925. Retrieved from <http://dx.doi.org/10.1029/1999JC000046> doi:
1486 10.1029/1999JC000046
- 1487 Schütte, F., Brandt, P., & Karstensen, J. (2016). Occurrence and characteristics
1488 of mesoscale eddies in the tropical northeast Atlantic Ocean. *Ocean Science*,
1489 12(3), 663–685.
- 1490 Smith, W., & Sandwell, D. (1997). Global Sea Floor Topography from Satellite Al-
1491 timetry and Ship Depth Soundings. *Science*, 277(5334), 1956–1962.
- 1492 Souza, J., Chapron, B., & Autret, E. (2014). The surface thermal signature and air-
1493 sea coupling over the Agulhas rings propagating in the South Atlantic Ocean
1494 interior [Journal Article]. *Ocean Science*, 10(4), 633-644.
- 1495 Souza, J. M. A. C., de Boyer Montégut, C., Cabanes, C., & Klein, P. (2011). Es-
1496 timation of the Agulhas ring impacts on meridional heat fluxes and transport
1497 using ARGO floats and satellite data. *Geophysical Research Letters*, 38(21).
1498 Retrieved from <http://dx.doi.org/10.1029/2011GL049359> (L21602) doi:
1499 10.1029/2011GL049359
- 1500 Stammer, D. (1997). Global characteristics of ocean variability estimated from
1501 regional TOPEX/POSEIDON altimeter measurements. *Journal of Physical*
1502 *Oceanography*, 27(8), 1743–1769.
- 1503 van Ballegooyen, R. C., Gründlingh, M. L., & Lutjeharms, J. R. E. (1994). Eddy
1504 fluxes of heat and salt from the southwest Indian Ocean into the southeast At-
1505 lantic Ocean: A case study. *Journal of Geophysical Research: Oceans*, 99(C7),
1506 14053–14070. Retrieved from <http://dx.doi.org/10.1029/94JC00383> doi:
1507 10.1029/94JC00383

- 1508 van Sebille, E., & van Leeuwen, P. J. (2007). Fast northward energy transfer in the
 1509 Atlantic due to Agulhas rings. *Journal of physical oceanography*, *37*(9), 2305–
 1510 2315.
- 1511 Wang, Y., Beron-Vera, F., & Olascoaga, M. (2016). The life cycle of a coherent
 1512 Lagrangian Agulhas ring. *Journal of Geophysical Research: Oceans*, *121*(6),
 1513 3944–3954.
- 1514 Wang, Y., Olascoaga, M., & Beron-Vera, F. (2015). Coherent water transport across
 1515 the South Atlantic. *Geophysical Research Letters*, *42*(10), 4072–4079.
- 1516 Weijer, W., De Ruijter, W. P., & Dijkstra, H. A. (2001). Stability of the Atlantic
 1517 overturning circulation: Competition between Bering Strait freshwater flux
 1518 and Agulhas heat and salt sources. *Journal of Physical Oceanography*, *31*(8),
 1519 2385–2402.
- 1520 Weijer, W., de Ruijter, W. P., Dijkstra, H. A., & Van Leeuwen, P. J. (1999). Im-
 1521 pact of interbasin exchange on the Atlantic overturning circulation. *Journal of*
 1522 *Physical Oceanography*, *29*(9), 2266–2284.
- 1523 Weijer, W., De Ruijter, W. P., Sterl, A., & Drijfhout, S. S. (2002). Response of the
 1524 Atlantic overturning circulation to South Atlantic sources of buoyancy. *Global*
 1525 *and Planetary Change*, *34*(3), 293–311.
- 1526 Williams, R. (2001). Ocean Subduction. In J. H. Steele (Ed.), *Encyclopedia of*
 1527 *ocean sciences* (p. 1982 - 1993). Oxford: Academic Press. Retrieved from
 1528 <http://www.sciencedirect.com/science/article/pii/B012227430X001094>
 1529 doi: <https://doi.org/10.1006/rwos.2001.0109>
- 1530 Wunsch, C. (1999). Where do ocean eddy heat fluxes matter? [Journal Article].
 1531 *Journal of Geophysical Research: Oceans (1978–2012)*, *104*(C6), 13235–13249.
- 1532 Zeitlin, V. (2018). *Geophysical fluid dynamics: understanding (almost) everything*
 1533 *with rotating shallow water models*. Oxford University Press.